Crustal structure of the rifted volcanic margins and uplifted plateau of Western Yemen from receiver function analysis

Abdulhakim Ahmed, Christel Tiberi, Sylvie Leroy, Graham Stuart, Derek Keir, Jamal Sholan, Khaled Khanbari, Ismael Al-Ganad, Clémence Basuyau

Title:

Crustal structure of the rifted volcanic margins and uplifted plateau of Western Yemen from receiver function analysis

Authors:

Abdulhakim Ahmed[1,2*],Christel Tiberi[3] ,Sylvie Leroy[2] ,Graham W. Stuart[4] ,Derek Keir[5] ,Jamal Sholan[1]

Khaled Khanbari[6] ,Ismael Al-Ganad[7] ,Clémence Basuyau[8]

Affiliations:

1 Seismological and Volcanological Observatory Center, Dhamar, Yemen.

2 Univ. Paris 06 CNRS ISTEP-UPMC, Paris, France.

3 CNRS Géosciences Montpellier, France.

4 School of Earth and Environment, University of Leeds, Leeds, United Kingdom.

5 National Oceanography Centre Southampton, University of Southampton, Southampton, United Kingdom.

6 Yemen Remote Sensing Center and Department of Earth and Environmental Science, Sana'a University Yemen.

7 Yemen Geological Survey & Mineral Resources Board, Sana'a, Yemen.

8 IPGP Paris

Accepted date: **Received date:**

Abdulhakim Ahmed,

ISTEP

UPMC, 4 place Jussieu 75252, Paris, Cedex 05, France

Phone: +33 14 42 73 40 8 Fax:+33 14 42 74 95 0 email: hakim66@myself.com

ABSTRACT

We analyse P-wave receiver functions across the western Gulf of Aden and southern Red Sea continental margins in Western Yemen to constrain crustal thickness and address the role of magmatism, faulting and mechanical thinning during continental breakup. We analyse teleseismic data from 21 stations (the temporary YOCMAL network together with GFZ and Yemeni permanent stations). Analysis of computed receiver functions shows that (1) the thickness of unextended crust on the Yemen plateau is ~35 km; (2) this thins to ~22 km in coastal areas and reaches less than 14 km on the Red Sea coast, where presence of a high velocity lower crust (HVLC) is evident. The average Vp/Vs ratio for the western Yemen Plateau is 1.79, increasing to ~1.92 near the Red Sea coast and decreasing to 1.68 for those stations located on or near the granitic rocks.

The crustal extension occurs over a ~130 km wide transition zone from the Red Sea and Gulf of Aden coasts to the edges of the Yemen plateau. Thinning of continental crust is particularly localized in a <30-km-wide zone near the coastline, spatially co-incident with addition of magmatic underplate at the base of the crust, potential seaward dipping reflectors (SDRs)_and thickened Oligo-Miocene syn-rift basaltic flows. Our results strongly suggest the presence of high velocity mafic intrusion in the lower crust. These bodies could have been associated with extension if intruded during the rifting, but they could also be a remnant of an upper mantle depleted during the eruption of the SDRs. Our results also point toward a regional breakup history in which the onset of rifting was synchronous along the western Gulf of Aden and southern Red Sea volcanic margins followed by a second phase of extension along the Red Sea margin.

Keywords:

Receiver function, volcanic margins, rifting, Red Sea, Gulf of Aden, western Arabia.

Introduction

During the breakup of continents, the lithosphere deforms by faulting, ductile stretching and thinning (McKenzie, 1978), and commonly also by magma intrusion in volcanic rifts (Ebinger & Casey, 2001; Buck, 2006). Despite the importance of breakup in plate tectonics we have few constraints on the spatial and temporal relationship between plate stretching and magma intrusion, and how these processes relate to the eruption of voluminous basalt flows that characterize magmatic margins worldwide (e.g., White *et al.*, 2008). We address this problem by imaging crustal structure (thickness and average seismic properties) using P-wave receiver functions (Burdick & Langston, 1977; Langston, 1977; Ammon, 1991) at the young (~30 Ma) Red Sea and Gulf of Aden rifted volcanic margins in the SW corner of Arabia, where the margin preserves the rift morphology resultant from breakup, and where the syn-rift geology and stratigraphic record has not yet been completely obscured by thick post-rift sediments (Davison *et al.,* 1994). Furthermore, the margin captures the change from magma-rich breakup in Western Yemen to magma-poor breakup in the eastern Gulf of Aden (Leroy *et al.,* 2010b), thus establishing a framework from which to interpret controls on the along-rift variability in melt supply.

Crustal thickness variations and the identification of magmatic input into the crust are key parameters in quantifying the locus and amount of tectonic stretching and associated thinning, as well as magmatic addition during continental rifting. We used 21 broadband seismic stations, the majority deployed for ~1 year (March 2009 – February 2010) along two profiles in Yemen that run perpendicular to the major

tectonic features in western Gulf of Aden, and southern Red Sea, and another profile parallel to the Red Sea coast to capture lateral variations in crustal thickness and internal properties along the rift margin (Fig. 1). We particularly focus on the relationship between magmatic intrusion, mechanical thinning, and the volcanic geology formed during the opening of these two rifts.

Tectonic Setting

The rifted margins of Yemen are located at the south-western corner of the Arabian Peninsula (Fig. 1), bounded to the west by the Red Sea and to the south by the Gulf of Aden. These two Oligocene spreading centres separate Arabia from the Nubia and Somalia plates, with the East African rift forming the third arm at the Afar triple junction (Fig. 1) (McKenzie *et al.*, 1970). Red Sea and Gulf of Aden rifting started in Oligocene times 30Ma ago, coeval with a peak in eruption of the voluminous Ethiopia-Yemen flood basalt province (e.g. Courtillot *et al.,* 1999; Ukstins *et al.,* 2002; Wolfenden *et al.,* 2005). The mean extension direction is oblique in the Gulf of Aden, which has an increasing extension rate from west (1.6 cm yr^{-1}) to east (2.3 cm yr^{-1})(Jestin *et al.,* 1994; Fournier *et al.,* 2001; Fournier *et al.,* 2010). The Red Sea has an extension rate that ranges from ~0.9 $cm.yr^{-1}$ in the north to ~1.5 $cm.yr^{-1}$ in the south (e.g. Jestin *et al.,* 1994; Chu & Gordon, 1998; Demets *et al.,* 2010). The opening in the southern Red Sea is more complex since the locus of strain likely shifted westward onland into Afar at ~11Ma (e.g. Chu & Gordon, 1998; Eagles *et al.,* 2002).

The presence of the Afar plume to the south has been used by Leroy *et al.,* (2010b) to explain the change from a magmatic margin in the west of the Gulf of Aden to a

poorly-magmatic margin in the east. Asthenospheric flow from the Afar plume has been proposed to explain the evolution of these rifts and the abnormal low mantle velocity beneath the rift and some of the Red Sea shoulders (e.g. Hansen *et al.,* 2007; Leroy *et al.,* 2010a; Chang *et al.,* 2011). Although the eastern Gulf of Aden margins, off-shore Oman, are described as magmatically poor, a post-rift magmatic activity exists as the base of the crust is underplated by a mafic body in some places (Lucazeau *et al.,* 2009; Autin *et al.,* 2010;Watremez *et al.,* 2011) and an upper mantle low velocity anomaly below the margin is reported (Basuyau *et al.,* 2010). Magmatic intrusion in to the Red Sea crust as well as the presence in the upper crust of salt (Davison *et al.,* 1994) affects the rheology of the crust and consequently its deformation both with strain localization and accommodation, and the amount of crustal thinning.

In southwestern Yemen the Proterozoic basement is unconformably overlaid by Permian Akbra shale, lower Jurassic Kohlan sandstone, upper Jurassic Amran limestone and Cretaceous continental Tawilah sandstones (Davison *et al.,* 1994; Beydoun, 1997). In the Tertiary the flood basalt volcanic trap series erupted and covered most of the study area to thicknesses of up to 3km(Fig. 2). On the ~40km wide Red Sea Tihama coastal plain the structural basement is overlaid by Miocene to recent clastics and evaporites up to ~4000 m thick (El- Anbaawy, 1992; Davison *et al.,* 1994) (Fig. 2). In the Gulf of Aden coastal plain, near Aden city syn-rift volcanic seaward dipping reflectors (SDR) are seen overlying the basement (Tard *et al.,* 1991; Leroy *et al.,* 2012).

Data and Methodology

During the seismological part of the YOCMAL project (e.g. Leroy *et al.,* 2010c), ~50 broadband seismic stations were distributed in three areas of Yemen (West, Central and East). In this paper we study the western area. The station distribution was designed to be perpendicular to the main axes of the two rifting systems: the Gulf of Aden and the Red Sea (Fig. 2). The seismic network was equipped with Guralp seismometers, 11 CMG-3ESP (60 s natural period) sensors, 36 CMG-6TD (30s natural period) sensors and 4 CMG-40T (30s natural period) sensors. The permanent GFZ station DAMY is equipped with STS-2 seismometer and Quantera-330 datalogger. Three stations of the Yemen permanent network are included (LBOS, BDHA and TRBA) - Fig. 2a. TRBA and BDHA are equipped with Mars-88 digitizers and LE3D sensors, while LBOS is equipped with Mars-88 digitizer and CMG-40T sensor. The temporary seismic stations were continuously recorded from March 2009 until February 2010 at 40 sps; DAMY records at both 100 and 20 sps; the Yemen network stations operated in trigger mode with a sampling rate of 62.5sps. All stations were equipped with a GPS timing system operated in continuous mode to synchronize the stations internal clock. Maintenance and data collection were carried out every 3 months during the recording period.

In this paper we study the western profile (Fig. 2), which can be divided into 3 sections: (1) A N-S section (Fig. 2a), which extends from the northern margin of Gulf of Aden up to Sana'a on the high plateau, has 9 stations (SANA, YSLE, RUSA, DAMY,

DAMT, KHLA, ADBA, DKUM, ADEN). (2) An E-W section in the north-west of Yemen, from the eastern margin of the Red Sea across the Tihama plain to Sana'a on the high plateau. This has 6 stations (SHIB, MAWI, TAWI, ANID, ZUWA and UAYA). (3) A 3 station section located parallel to the southern Red Sea coast consists of SUGH, KHAW and MOKA.

During the operation period of the network, > 100 earthquakes within the teleseismic epicentral distance range (25^0-95^0) and with Mw >5.5 were recorded. Based on the signal-to-noise ratio, we selected the best waveform data recorded at each station. The number of events included in the final analysis varies from 10 to 47 per site (Table 1), depending on the background noise and the state of health of the station. Most of the selected events come from the ENE backazimuth with some events from the south and from the northwest (Fig. 2b). A lack of large magnitude earthquakes from southerly backazimuths (150^0-300^0) results in an inhomogeneous distribution of events and hence insufficient data for detailed analysis of crustal anisotropy using receiver functions (e.g. Frederiksen *et al.,* 2003).

The waveform of teleseismic P-waves, recorded at three-component broadband stations, is dependent on the instrument response, source radiation pattern, propagation path and local crustal structure beneath the station. By removing the effects of the source, propagation path and instrument response using the receiver function technique (e.g. Langston 1977, 1979), the information of the local crustal structure beneath the station can be derived from P-wave to S-wave conversions (0wens *et al.,* 1984; Ammon 1991). In this study, we use the iterative time domain

deconvolution technique, developed by Ligorria and Ammon (1999), to compute receiver functions.

We filter our raw waveforms with a zero phase Butterworth bandpass filter with corner frequencies of 0.02 - 0.8 Hz. The N-S and E-W horizontal components are rotated to radial and tangential components. A 30s time window (5s before the theoretical P arrival time and 25s after) is used to deconvolve the vertical component from the radial and transverse to calculate the receiver functions. Following Ligorria and Ammon (1999), we apply a Gaussian filter of 2.5 s to the deconvolved spike wave train, except for the noisiest stations where a Gaussian width of 2.0 is used.

Crustal thickness (H) and the average crustal Vp/Vs ratio (k) are initially determined using the H-k domain stacking technique (Zhu & Kanamori, 2000). There is an inherent trade-off in receiver function analysis between crustal thickness and average crustal velocity properties (Ammon *et al.,* 1990). The H-k stacking algorithm reduces this ambiguity by summing amplitudes of the receiver function for Moho P-to-S conversion Ps and its multiple converted phases, PpPs and PpSs+PsPs (Fig. 3e) at predicted arrival times using different crustal thickness H and Vp/Vs values.

The stacking amplitude in the H-k domain is then given by:

$$s(H,K) = \sum_{m=1}^{n} \mathrm{W}_1 r_m(\mathrm{t}_{P_s}) + \mathrm{W}_2 r_m\left(t_{P_pP_s}\right) - \mathrm{W}_3 r_m\left(t_{P_pS_s+P_sP_s}\right) \qquad (1)$$

Where n is the number of receiver functions, $\mathrm{W_j}$ is a weighting factor that represents the contribution of the corresponding seismic phase according to signal-to-noise

ratio (W_1+ W_2+W_3 = 1) and $r_m(t)$ is the amplitude of the receiver function at time t of the associated seismic phase. When the three phases stack constructively, s(H,k) reaches its maximum; this represents the best estimate for both H and Vp/Vs (k) beneath the station. The weighting factors used in this study for most of the stations are W_1=0.6, W_2=0.3, W_3=0.1 (Zhu & Kanamori, 2000). Only in few cases, when the Moho conversion phase amplitude is low or when high amplitude intra-crustal interfaces conversion phase obscured the Moho Ps conversion, did we modify the weighting factors. We choose a value of 6.2 $km.s^{-1}$ for average crustal P-wave velocity (Vp), in agreement with previous controlled-source seismic work in the region (e.g. Egloff *et al.,* 1991). We estimate the standard deviation for both crustal thickness H and Vp/Vs ratio with a bootstrap re-sampling technique (Efron & Tibshirani, 1986). The bootstrap analysis was done for random subsets of data for each station, and the dispersion of the result gives the error bars mentioned in the depth sections. We applied the same technique to estimate the error coming from the average P-wave velocity used in the inversions (Tiberi et al.2007). Another advantage of this (H,k) stacking method is that it gives an indication of average crustal composition with a local estimate of Vp/Vs value (e.g. Christensen, 1996). This ratio is related to the Poisson's ratio through a simple relationship (Zandt & Ammon, 1995; Ligorria, 2000), and its variations depend on crustal mineralogy (felsic, mafic), the presence of fluids and physical properties of the rocks.

To refine our crustal model into upper and lower crustal layers, we invert a stack of the radial receiver functions with a stochastic method (Shibutani *et al.,* 1996). We use the Neighborhood Algorithm (NA) technique (Sambridge, 1999a, 1999b) to

invert for a 1D crustal shear wave velocity-depth distribution beneath a number of our sites. The initial model is based on wide-angle reflection and refraction seismic profiling results (e.g. Egloff *et al.,* 1991, Fig. 2), and the Vp/Vs ratio is estimated from H-k stacking results. We invert for a model, which is composed of 4 to 5 layers: a sediment layer, when needed, basement, upper crust, lower crust and uppermost mantle. In each layer the model parameters are layer thickness, shear wave velocity at the upper and lower boundaries of the layer and the layer Vp/Vs ratio. The receiver function parameterization and calculation follow the one implemented by Shibutani *et al.,* (1996).

Results

Our crustal model results, tabulated in Table 1, exclude the stations DABI, MARA, HOTA and HQBA (Fig. 2a), due to their malfunction, which resulted in inadequate data for receiver function analysis. Hereafter we use the term Moho depth as a representative of crustal thickness (H) below the station.

N-S section from Sana'a to Gulf of Aden

Crustal thickness for all the stations located on the plateau (SANA, YSLE, RUSA, DAMY, DAMT) is 35 km +0.5 km (Table 1, Fig. 3a). The identified Moho Ps conversion phase by the inversion appears between 4.83 and 4.93 s after the first arrival (Fig. 3a). The associated Vp/Vs for these plateau stations ranges from 1.76 (RUSA) in the middle of plateau to 1.83 (DAMT) in the southern edge of the plateau. Such values are typical of felsic to intermediate composition crust (Christensen,

1996). DAMT station is located in a hydrothermally active area resulting in deep circulation of the surface water, which is heated and returns back to the surface as steam and/or hot water (Fara et al., 1999; Alderwish, A. and Almatary, H., 2012). The high value of Vp/Vs for this station may be related to high porosity, the presence of water and gases in the upper few kilometers of sedimentary and volcanic rocks.

At some stations (e.g. SANA), a strong positive peak, attributed to an intra-crustal interface, can be observed before the Moho conversion Ps phase (Fig. 3a). For SANA station, we interpret this arrival as an intra-crustal discontinuity approximately located 21 km below the station (Figs. 3, 4 and 5). DAMY seems to have a shallower interface, as a similar peak is observed at 0.83 s delay time (< 5 km depth, see supplementary material).

KHLA has an estimated crustal thickness of ~34 km (Vp/Vs of 1.75), slightly thinner than that to the north. The error estimate for this station is large (±6 km and ±0.09 for H and k, respectively) due to a weak Moho conversion phase Ps peak and numerous multiples for events approaching the station from the east. ADBA, further south, has a 31 km ±1.78 km crust associated with an average crustal Vp/Vs of 1.68 ±0.053 (Fig. 5).

The southern end of the profile is characterized by a thinner crust (23.6 km and 20.4 km for DKUM and ADEN, respectively). These receiver functions also show a smaller amplitude Moho Ps conversion phase, implying a reduced impedance contrast across the Moho, especially for events approaching from the east (Fig. 3a, 6b & 6d). The Vp/Vs are 1.69 and 1.73, for DKUM and ADEN, respectively. At ADEN station, we

observe a high amplitude intra-crustal conversion at 1.85 s (~11Km) for all events with a backazimuth less than N106º. This peak arrives earlier for more northerly azimuths as shown in Fig. (6b).

To further our understanding of the crustal layering along this section we invert the receiver function waveforms for ADEN, ADBA, DAMT, RUSA and YSLE using the NA algorithm, as all of these stations show intra-crustal phases on their receiver function waveforms. Examples of inversion results are shown in Fig. (7). We obtain crustal thicknesses comparable to those from Zhu & Kanamori (2000) technique. ADBA has a complex crustal structure (Figs 4 and 8), with the inversion (Fig. 8) producing a low velocity lower crust beneath the station, not observed on other stations. However, testing different forward models, the best fit is obtained for a model including a thin intracrustal layer with both high P-wave velocity and Vp/Vs ratio (Fig. 8c and d), rather than a low velocity lower crust. We favour this model and interpret this high velocity layer as a horizontal igneous intrusion (sill) into the crust.

For the Yemen permanent network stations located to the east of the N-S section of the profile (LBOS and BDHA, Fig. 2) we find 32.6km and 36.2km crustal thickness with 1.83 and 1.76 Vp/Vs ratio, respectively. These values are consistent with the ones found for KHLA and ADBA.

E-W section from the Red Sea coast to Sana'a

The receiver functions of stations SHIB, TAWI, UAYA, ZUWA, ANID, and MAWI are characterized by complex waveforms (Figs 3 and 4). For SHIB, TAWI and MAWI, the

H-k stacking method gives a crustal thickness of 31 to 35km, decreasing westward with a crustal Vp/Vs ratio around 1.8. Earlier peaks are observed at SHIB, MAWI (2.66s and 2.21s, respectively) and to a lesser extend for TAWI. They are interpreted in terms of intracrustal interfaces. We also note two later arrivals for these stations at about 6-8s and 10-11s, that cannot be modelled as multiples from shallower interfaces (Fig. 4). These are possibly upper mantle discontinuities, which need further investigation but are outside the remit of the present paper.

On the sediments of the Tihama plain (ANID, ZUWA and UAYA), the receiver functions become more complex (Figs 3b, 4 and 9b,c) due to conversions and multiples from the thick sediment layers, which include salt, covering the area. We stack 23 events for ANID station, located at the eastern end of Tihama coastal plain and observe three positive peaks at 1.75s, 3.3s and 6.95s delay times (Fig. 4). The first peak is interpreted as an intra-crustal phase, and in this case, the third one could be a multiple of the first; the second one is interpreted as the Moho conversion phase. It gives a crustal thickness of 22.8 km and a Vp/Vs value of 1.83 (Figs 4 and 5).

ZUWA station shows two main features. First, the low amplitude of the first P compared to the following Ps conversion (fig. 9c) comes from the sediment-bedrock interface beneath the station. Second, we observe a clear shift of Moho Ps conversion between events with easterly backazimuths (< 106º) and events with westerly backazimuths (>140º). We can explain this by the fact that ZUWA is located near a N-S normal fault, implying an azimuth dependent velocity structure. For azimuths <106º, seismic structure will be similar to ANID case (Vp=6.2 $km.s^{-1}$),

whereas for azimuths >140º, it will be similar to UAYA station. For the latter case, we base our choice on Egloff et al. (1991) study (profile VI) and take an average Vp of 5.3 km.s^{-1} (4 km of sedimentary layer). We then proceed to two separate inversions, and in both cases we obtain the best result for a crustal thickness of 23 km, consistent with the value obtained for the nearby station ANID. The corresponding Vp/Vs ratios are 1.91 and 1.95 for azimuths >140º and <106º, respectively (fig. 9c). These are the highest values of Vp/Vs ratio we obtain for all the stations. We relate it to sedimentary deposits in Tihama basin (El-Anbaawy, 1992; Egloff *et al.,* 1991; Davison *et al.,* 1994).

UAYA, located along the Red Sea coast, has numerous high amplitude conversion phases prior to the Moho Ps within a very small time window of 2.27 s (Fig. 9b). However, there are two dominant conversion phases one at 1.3s and the other at 2.3 s, with multiples at 5.3s, 6.6s and 7.3s, 10s respectively. The first one is a conversion phase at an intra-crustal interface at about 9.6 km depth when using an average upper crustal velocity Vp of 4.5 km.s^{-1} (Egloff et al., 1991), while the second one is the Moho conversion phase. Based on our estimate of the average velocity for the crust from the results of seismic profile VI of Egloff et al. (1991) near the coast of the Red Sea, we obtain a crustal thickness of 13.8 km with a Vp/Vs ratio of 1.92 (Vp = 5.3 km.s^{-1}).

Stations adjacent to the Red Sea coast

For the Red Sea coast stations SUGH, KHAW and MOKA (Fig. 2) we find a stable crustal thickness estimate varying between 21 to 23 km (Table 1). The estimated

Vp/Vs for these 3 stations is 1.73, 1.68 and 1.85 respectively. KHAW station has the lowest Vp/Vs ratio of the three (1.68). Sedimentary layering obviously affects KHAW signal (trough at 2s following the positive peak at 0.5s, Figs 3c and 4). The MOKA receiver function contains two high amplitude Ps conversions at 1.2s and 1.88s (fig. 3c). The first one happens at the base of a low velocity sediment layer. The second one corresponds to the interface between the upper and lower crust modified by high velocity mafic intrusion (Vp/Vs = 1.85). The Moho Ps conversion phase is characterized by a very low amplitude for this station thought to be due to a reduction in the impedance contrast across the boundary due to the high velocity lower crust.

For TRBA station, we estimate the crustal thickness to be 27.4 km with a Vp/Vs ratio of 1.86. A shallow interface can also be deduced from a weak amplitude Ps conversion at 0.85s delay time (Fig. 3d), while the interface between the upper and lower crust cannot be seen. This is comparable to the results of the stations located on the volcanic trap series south of SANA.

Imaging the crustal structure by migration of receiver functions

Migration of receiver functions from the time domain to the space domain is a common technique to image the continuous variations of the structures beneath a receiver function profile (e.g. Kind *et al.,* 2002). In this study, we use the common conversion point (CCP) stacking technique of Zhu (2000). A bin size of 20 km wide, 5 km long and 0.5 km vertically is used. The choice of these parameters balances

between the resolution of the interfaces and their continuity. The migrated cross sections have been created using IASP91 velocity model (Kennett & Engdahl, 1991). Figure 10 displays the migrated receiver functions along the N-S and E-W sections. As a comparison, the inverted Moho depth (referred to sea level) using the H-k stacking method of Zhu & Kanamori (2000), are plotted as black dots with error bars from the bootstrap technique.

The Moho discontinuity is associated with a strong positive amplitude (red colour; Fig. 10), which diminishes in amplitude as one moves towards the coast. For the N-S profile, the Moho interface is sub-horizontal between SANA and DAMT at an approximate depth of 35 km. At the southern end of the profile, the Moho is at a depth of ~20 km beneath ADEN. Between ADBA and DKUM ~7.5 km of crustal thinning happens over 32 km lateral distance. The intra-crustal interface between 15-21 km, interpreted here to be the upper/lower crust boundary, is observed between SHIB and SANA, and then between DAMT and ADBA stations. The change in the character of this intra-crustal boundary between SANA and DAMT may be explained by lateral variations in crustal composition.

In the E-W migrated receiver function profile, the Moho discontinuity is clear and lies at a depth of 35 km at the eastern end of the profile. It then rises steeply in two stages at the western end to reach ~14km beneath UAYA. The first stage of crustal thinning occurs between MAWI and ANID (~8.6 km vertically over 34 km horizontally). The second stage of thinning comes between ZUWA and UAYA (~9.2 km vertically over 30 km horizontally). A clear positive phase is observed along the section in the east from 21 km depth (SANA) up to 9.6 km (UAYA), which

corresponds to a clear crustal conversion in the signal for all stations. This conversion is weak at TAWI and is smeared between TAWI and MAWI (see individual RF's in the supplementary material). We interpret it to be the interface between the upper and lower crust.

Discussion

Thinning of the crust

Our crustal thickness estimates range between 20 and 23 km in the coastal areas, with the exception of UAYA, right on the Red Sea coast with a crustal thickness of ~14 km and between 35-36 km below the Yemen plateau. These are comparable to the results from other studies of the western Arabian Plate shown in Fig. 11 (Al-Damegh *et al.,* 2005; Hansen *et al.,* 2007; Mooney *et al.,* 1985).

The 1988 SONNE seismic line from the Red Sea coast to the Yemen plateau estimated the crust to be thicker in the coastal areas and thinner below the plateau than our results (Egloff *et al.,* 1991, Fig. 2). Makris *et al.,* (1991), from a gravity interpretation, estimates the crust to be 35 km below Sana'a and 22 km below Tihama plain, which is consistent with our results, and also implies that the entire area is isostatically compensated.

Our crustal thickness beneath the Yemen Plateau (~35km) corresponds to the lower bound of the Ethiopian Plateaus crustal thicknesses (between 35 and 45 km, Stuart et al., 2006; Bastow & Keir, 2011; Hammond et al., 2011) Fig. (11). Our lowest value beneath UAYA (~14km) is very close to the one obtained in the Danakil depression

(Hammond et. al. 2011) Fig.(11), where mafic intrusions are also likely to take places (e.g. Tiberi et al., 2005).

There is a clear mid-crustal interface at depths between 10-21 km along the E-W profile (Fig. 10) as well as at stations located to the east of Yemen volcanic trap series (DAMT, KHLA, ADBA, LBOS and BDHA). We interpret this interface to be the upper/lower crust boundary - the Conrad discontinuity. This discontinuity is caused by a sharp velocity step separating the upper crust (average Vp of 6.3 $km.s^{-1}$) from the lower crust (average Vp of 7.0 $km.s^{-1}$) (e.g. Mooney *et al.,* 1985; Egloff *et al.,* 1991). Such an interface seems to be a common feature for the Arabian plate (Mooney *et al.,* 1985; Egloff *et al.,* 1991; Stern & Johnson, 2010). Stern & Johnson (2010) suggest that it separates slower felsic upper crust from faster mafic lower crust, and may coincide with the transition from brittle to ductile deformation. For those stations located on the Yemen volcanic trap series (YSLE, RUSA, DAMY and TRBA), south of Sana'a (Fig. 10) and also KHAW on the Red Sea coast, the Conrad discontinuity is not imaged by our receiver functions. This implies the crust was modified by magma intrusion during the Oligo-Miocene flood basalt volcanism caused by the impact of the Afar plume 30 Ma ago (Baker *et al.,* 1994), and decompression melting of hot mantle during rifting. The shallower interface below those stations (1-4 km depth) is interpreted as the boundary between basement and the overlaying thick sedimentary and/or volcanic cover.

The onset of crustal thinning on the Gulf of Aden margin starts somewhere between KHLA and DAMT and ends between ADBA and DKUM (Fig. 10). This implies one stage of thinning (7.4 km vertically over 32 km horizontally). If we assume the

average initial crustal thickness to be 35 km (SANA) and the final extended crust for the coastal areas to be 22 km (ADEN), the β stretching factor works out to be about 1.6. This only gives a lower bound as mafic intrusions maintain crustal thickness during extension. An upper bound for the stretching factor is obtained by only considering the upper 12 km as non-intruded crust beneath ADEN, to gives β ~3.

On the Red Sea margin, however, the situation is more complex. If we consider the extended crustal thickness to be that of UAYA (13.8 km), we obtain a stretching factor as high as 2.5, which is slightly higher than the maximum value reported beneath the Red Sea, offshore Yemen (β≈2.4, Davison *et al.,* 1994). Moreover, we observe two rapid changes in the crust thickness (Fig. 9 & 10). The first one happens between the plateau (h~35 km) and the coastal plain (h~ 22 km) . The second step is located between ZUWA and UAYA stations, where the crustal thickness decreases sharply from h~ 22 km at the coastal plain to 13.8 km at UAYA over ~30 km. The lower bound of β factor estimate is then ~1.6 for both steps in crustal thickness, similar to the Gulf of Aden margin, and comparable with the results for the stretching factor calculated from geometry of fault block rotations (Davison *et al.,* 1994). When comparing the 35 km thick non-extended crust beneath SANA and the present 14 km beneath UAYA, we obtain a maximum β of 2.5. A similar value (2.4) is obtained between UAYA and ZUWA when considering that mafic intrusion maintained the crustal thickness and thus overestimates its value beneath UAYA (14 instead of 9.5 km). Two stages of crustal extension should be then considered for the Red Sea margin.

Crustal Underplating (high velocity lower crust -HVLC)

On the Red Sea coast UAYA has a strong intra-crustal interface at 9.6 km depth with clear multiples, and a Moho discontinuity at about 13.8 km (Fig. 9). Our crustal thickness estimate is consistent with the 11-14 km obtained further south near Al-Hudaidah (Fig. 2) during the SONNE experiment (Egloff *et al.,* 1991). Considering local isostasy with an average crustal density of 2670 $kg.m^{-3}$ and a mantle density of 3300 $kg.m^{-3}$, the Moho should be at ~22 km depth beneath UAYA. The presence of seaward dipping reflectors (SDR) in this region (Davidson *et al.,* 1994) and our results suggest the presence of a high velocity lower crust (HVLC, Fig. 9). Consequently, we conclude that the area is underplated by a high velocity dense material resultant from the ~11Ma rifting episode (Eagles *et al.,* 2002). This explains both a thinner crust and the complexity of the signal beneath UAYA. North of UAYA at the western end of the Saudi Arabian refraction profile (between shot point 5 ~17.77N, 42.35E and shot point 6~16.57N, 42.06E) there is evidence of a double-layered Moho overlain by a sedimentary basin containing salt deposits (Mooney *et al.,* 1985; Milkereit & Fluh, 1985; Prodehl, 1985). Further south along the Red Sea coast, there is no evidence of a similar HVLC either from seismic profile near Al-Hudaydah (Egloff *et al.,* 1991) or from our receiver function results at KHAW. However at MOKA (Fig. 2) a complex receiver function is found similar to that at UAYA with high amplitude intra-crustal multiple conversion phases and a low amplitude Moho Ps conversion phase with its associated multiples (Fig. 3c). This receiver function waveform together with the existence of Miocene volcanism in Jabal An Nar near MOKA (Capaldi *et al.,* 1987) may indicate the presence of local

underplating. Such isolated off-axis underplated volcanoes have been reported at eastern Gulf of Aden continental margin (Lucazeau *et al.,* 2009; Autin *et al.,* 2010; Watremez *et al.,* 2011).

On the Gulf of Aden coast, we interpret the intracrustal interface we found at 11 km (Fig. 6) to be an intrusion of igneous material at the base of the lower crust. This causes weak impedance contrast between the lower crust and the mantle, thus explaining the low amplitude Moho Ps conversion phase observed (Fig. 6). However, this HVLC produces a high impedance contrast with the overlying upper crust, causing the high amplitude conversion phase we observe at ~2s in Fig. 6. The thickness of the HVLC works out to be ~9 km from these observations. Tard *et al.,* (1991) identified syn-rift seaward dipping reflectors in this area. We thus conclude that this margin is a typical volcanic margin (e.g. Leroy *et al.,* 2012).

Our observations and previous studies (volcanism, tectonics, geochronology; e.g. Bosworth *et al.,* 2005) suggest that the onset of rifting along the western Gulf of Aden and the Southern Red Sea was synchronous. From our results in UAYA, we propose a second phase of thinning confined to the Red Sea which has been suggested in previous studies (e.g. Girdler *et al.,* 1974). This rifting phase could have occurred after the deposition of the halite deposits and during the initiation of new oceanic crust in the southern end of the Red Sea axial trough (Egloff *et al.,* 1991). In this case, the timing of the halite deposition (syn or post-rift, Fig. 9) and the dating of the Yemeni granite intrusions (Hughes & Beydon, 1992; Davison *et al.,* 1994; Geoffroy *et al.,* 1998, Fig. 2) need clarifying.

The crustal characteristics of the western Yemen volcanic rifted margin can be recognized in other volcanic margins (Menzies *et al.,* 2002; Direen *et al.,* 2008). (1) The pre-rift Oligio-Miocene flood basalt volcanism (Yemen Trap Series) which could be related to Afar plume activity ~30 Ma, can be compared to south Atlantic volcanic margins with the emplacement of pre-rift Paraná-Etendeka flood basalt, for example the Namibia volcanic margin (Gladczenko *et al.,* 1998); (2) A 50-70 km wide volcanic margin transition zone from extended modified continental crust to true oceanic crust is similar to the one found in the North Atlantic at the Hatton Bank volcanic margin (Smith *et al.,* 2005), and the narrower 10-40 km wide extended zone reported for Møre volcanic margin (Mjelde *et al.*, 2009). In the South Atlantic (Nambia) and western Australia wider ~150-200 km extended zones have been interpreted (Bauer *et al.,* 2000; Gladczenko *et al.,* 1997; Gladczenko *et al.,* 1998; Direen *et al.,* 2008); (3) On the eastern coast of the Red Sea most of the syn-rift and post-rift mafic dykes , which parallel the Red Sea margin, are concentrated along the Tihama plain escarpment area (Mohr, 1991). On the plateau, in the Aden traps of Dhala, Musaymir and Radfan the dike trends are variable from NW to NE (Moseley, 1969; Mohr, 1991), while most of the dykes along Aden volcanic line are in an EW direction parallel to the Gulf of Aden rift (Cox *et al.,* 1970); (4) In the Gulf of Aden seaward dipping reflectors (SDR's) overlie most of the extended zone and thicken seaward (Tard *et al.,* 1991; Leroy *et al.,* 2012). Seaward dipping reflectors are one of the distinguishing features of volcanic margins and have been imaged in seismic profiles on Labrador Sea (Keen *et al.,* 2012), Namibia (Bauer *et al.,* 2000) and Exmouth–Gascoyne margin western Australia (Rey *et al.,* 2008) volcanic margins.

(5) High velocity lower crust (HVLC or underplating) is an important feature of volcanic margins and has been identified for both the Red Sea and Gulf of Aden margins (e.g. Milkereit & Fluh, 1985; Prodehl, 1985). HVLC's exist in Exmouth–Gascoyne, Namibia, Møre, Hatton Bank and Vøring typical volcanic margins (Rey *et al.,* 2008; Bauer *et al.,* 2000; Mjelde *et al.,* 2009; Smith *et al.,* 2005; Gernigon *et al.,* 2004). (6) Oceanic crust at the axial trough of Red Sea and along Gulf of Aden spreading center has been reported by many studies (e.g. Girdler & Underwood, 1985; Bosworth *et al.,* 2005; Leroy *et al.,* 2012). In the Red Sea 4 km thick oceanic crust is reported in the central part of the axial trough and 1-3 km thick of new oceanic crust is estimated for the southern part north of 15.5^0N latitude (Girdler, 1991; Egloff *et al.,* 1991). For Gulf of Aden the oceanic crust is thicker ~8 km and covers a wider area on the two flanks reaching isochron A5 in the east and A4 in the south of Aden (Hebert *et al.,* 2001; Leroy *et al.,* 2012, Fig. (6)).

Vp/Vs ratio and crustal composition

Most of the stations are characterized by felsic to intermediate composition crust with Vp/Vs in the range of $1.73 \leq k \leq 1.86$ (Christensen, 1996) (Table 1). This average Vp/Vs is a whole crust result and with the presence of the mid-crustal discontinuity suggests a mafic composition for the lower crust, which has been altered by Miocene-Oligocene extensive volcanism. It is difficult to determine how the lower crust has been altered, whether by intruded material from the mantle or by another alteration process (Baker et al. 1998) given only Vp/Vs ratios. However

the seismic refraction profiles in Saudi Arabia and Yemen confirm this crustal division and show an average Vp of 6.3 $km.s^{-1}$ for the upper crust and 7.0 $km.s^{-1}$ for the mafic lower crust (Mooney *et al.*, 1985; Egloff *et al.,* 1991). Stern *et al.,* (2010), described the lower crust beneath Arabian shield to be broadly gabbroic in composition with the possibility of second-order compositional variations such as increased plagioclase content upwards and increased pyroxene content downwards. They also concluded that most of the Arabian shield upper crust was formed by magmatic additions at intra-oceanic arcs above several past subduction zones (870-630 Ma) with post-tectonic subordinate granitic and volcanic rocks contributing to the growth of the Arabian shield.

Hammond *et al.,* (2011) ascribed the Vp/Vs ratio variation (1.7 – 1.9) for western Ethiopian plateau to mafic crust altered by the Cenozoic volcanism, whereas the south-eastern plateau shows more typical silicic continental crust with a Vp/Vs ratio of 1.78. Dugda *et al.,* (2005), concluded that the crustal structure on the western side of Ethiopian plateau has not been altered by Cenozoic volcanism as the Moho depth and average Vp/Vs ratio are comparable to unmodified Mozambique Belt crust in Tanzania and Kenya and similar to the global average for Precambrian crust. Our results from the Yemen plateau show that low Vp/Vs values (~1.68) characterise stations located on the granitic intrusions or on the Precambrian quartz-rich rocks.

For the Red Sea coastal area west of ZUWA station, the Vp/Vs ratio is greater than 1.90. High values in this area could reflect sedimentary infill (Fig. 9). The presence of a HVLC beneath UAYA increases the Vp/Vs ratio (1.92) due to its mafic nature

(Watanabe, 1993; Christensen, 1996). The complex receiver function in the presence of a HVLC and the high Vp/Vs ratio values near the Red Sea coast give strong evidence for a different amount of extension in this area. In contrast the lower Vp/Vs of 1.73 for ADEN station is not expected in a basalt volcanic field. This low Vp/Vs value might suggest the existence of water in the crust. Watanabe (1993) concluded that as the fluid fraction increases to 10 vol.% in case of water, the Vp/Vs will decrease though in case of molten rocks it will increase.

Conclusion

From a detailed study of the receiver functions through a profile in Western Yemen, we were able to:

1) map the Moho depth variations both for the Gulf of Aden and Red Sea margins. The crustal thickness beneath the Yemen Plateau is ~35 km consistent with values obtained elsewhere on the Arabian peninsula. The thickness decreases to 22 km for the coastal regions of the Aden rift and to less than 15km for the Red Sea. The lower-bound stretching factors we deduced are ~1.6 for both rifts, implying a coeval rifting history, except in the UAYA region where our results strongly suggest that a second phase of rifting with the same stretching factor has occurred after the deposition of halite deposits.

2) image intracrustal discontinuities beneath a number of stations. One of these interfaces is interpreted as the Conrad discontinuity, separating the upper

from the lower crust. It is particularly well imaged beneath the stations located along the E-W section and is not visible in regions of extensive volcanism to the east. Near the coastal areas, the shallowest interfaces may be related to the sediment-basment contact.

3) confirm that the two volcanic margins of western Gulf of Aden and southern Red Sea are underplated by high velocity dense material at the base of lower crust (HVLC). The HVLC is overlain in the upper crust by seaward dipping reflectors evidenced in previous seismic profiling studies.

4) estimate the crustal composition from Vp/Vs ratio as altered mafic lower crust and felsic upper crust beneath the plateau and southern part of the profile. For those stations located on or near granitic bodies the crust is more silicic. Regions overlain by sedimentary basins have modified thinned lower crust.

Acknowledgements

We gratefully acknowledge Francis Lucazeau, Elia d'Acremont, Fredrique Rolandone, Alex Brisbourne and David Hawthorn (NERC Seis-UK equipment pool), the French Embassy in Yemen (J. G. Sarkis, J. Dechezlepretre and C. Bousquet) , local governers and the people of the Yemen governerates for their help during the field work. We thank Jérôme Vergne and Gyorgy Hetenyi for providing the CCP migration software. We thank two anonymous reviewers for their positive suggestions

improving the manuscript. The work was funded by the Agency National de la Recherche YOCMAL project, CNRS-INSU-PICS Yemen, GSMRB Yemen and Actions Marges.

References:

Al-Damegh, K., Sandoval, E. & Brazangi, M., 2005. Crustal structure of the Arabian plate: new constraints from the analysis of teleseismic receiver functions. Earth Planet. Sci. Lett., 231, 177–196.

Alderwish, A and H. Almatary, H. (2012). Hydrochemistry and thermal activity of Damt region, Yemen. Environmental Earth Sciences, 65(7):2111-2124.

Ammon, C. j., Randall, G. & Zandt, G., 1990 "On the Nonuniqueness of Receiver Function Inversions," J. Geophys. Res., Vol. 95, pp.15303-15318.

Ammon, C. J., 1991. The isolation of receiver effects from teleseismic P waveforms, Bull. Seism. Soc. Am., 81, 2504-2510.

Autin, J., Leroy, S., Beslier, M. O., d'Acremont, E., Razin, P., Ribodetti, A., Bellahsen, N., Robin, C. & Al-Toubi, K., 2010. Continental break-up history of a deep magma-poor margin from seismic reflection data (northeastern Gulf of Aden margin, offshore Oman). Geophys. J. Int., 180, 501-519.

Baker, J., Menzies, M. & Snee, L., 1994. Stratigraphy, 40Ar/39Ar geochronology and geochemistry of flood volcanism in Yemen. Mineralogical Magazine, 58A, 42–43.

Baker, J. A., Thirlwall, M. F. & Menzies, M. A. , 1996. Sr-Nd-Pb and trace element evidence for crustal contamination of plume-derived flood basalts: Oligocene flood volcanism in western Yemen. Geochimica et Cosmochimica Acta 60, 2559-2581.

Baker, J. A., Menzies, M. A., Thirlwall, M. F. & Macpherson, C. G., 1997. Petrogenesis of Quaternary intraplate volcanism, Sana'a, Yemen: implications for plume-lithosphere interaction and polybaric melt hybridization. J. of Petrology 38, 1359-1390.

Baker, J., Chazot, G., Menzies, M. & Thirlwall, M., 1998. Metasomatism of the shallow mantle beneath Yemen by the Afar plume.implications for mantle plumes, flood volcanism, and intraplate volcanism. Geology 26, 431-434.

Bastow, I. D. & Keir, D., 2011. The protracted development of the continent–ocean transition in Afar. Nature Geoscience, 4, (4), 248-250. (doi:10.1038/ngeo1095)

Basuyau, C., Tiberi, C., Leroy, S., Stuart, G., Al-Lazki, A., Al-Toubi, K. & Ebinger, C. 2010. Evidence of partial melting beneath a continental margin: case of Dhofar, in the Northeast Gulf of Aden (Sultanante of Oman). Geophys. J. Int., 180,520-534.

Bauer, K., Schreckenberger, S.N., Emmermann, B., Hinz, K., Fechner, N., Gohl, K., Schulze, A., Trumbull, R.B. & Weber, K., 2000. Deep structure of the Namibia continental margin as derived from integrated geophysical studies. J. Geophys. Res., 105, 25,829–25,853.

Beydoun, Z. R., 1997. Introduction to the revised Mesozoic stratigraphy and nomenclature for Yemen. Marine and Petroleum Geology, 14, 617-629.

Bosworth, W., Huchon, P. & McClay, K., 2005. The Red Sea and Gulf of Aden basins. J. Afr. Earth Sci., 43, 334–378.

Buck, W. R., Einarsson P. & Brandsdottir, B., 2006. Tectonic stress and magma chamber size as controls on dike propagation: Constraints from the 1974-1989 Krafla rifting Episode, J. Geophys. Res. 111; B12, B12404.

Buikin, A. I., Trieloff, M., Korochantseva, E. V., Hopp, J., Kaliwoda, M. , H.-P. Meyer, H. P. and R. Altherr R., 2010. Distribution of Mantle and Atmospheric Argon in Mantle Xenoliths from theWestern Arabian Peninsula: Constraints onTiming and Composition of Metasomatizing Agents in the Lithospheric Mantle. J. of Petrology 51, 2547-2570.

Burdick, L. J. & Langston, C. A.,1977. Modeling crustal structure through the use of converted phases in teleseismic body waveforms. Bull. Seism. Soc. Am., 67, 677-692.

Capaldi G., Manetti P., Piccardo, G.B., Poli G., 1987. Nature and geodynamic significance of the Miocene dyke swarm in the North Yemen (YAR). Neues Jahrb. Mineral., Abh., 156, 207–229.

Chang, S.-J., Merino, M., Van der Lee, S., Stein, S., & Stein, C., 2011. Mantle flow beneath Arabia offset from the opening Red Sea, Geophys. Res. Lett., 38, L04301.

Chang, S.-J. & Van der Lee, S., 2011. Mantle plumes and associated flow beneath Arabia and East Africa. Earth Planet. Sci. Lett., 302, 448-454.

Christensen, N.I., 1996. Poisson's ratio and crustal seismology. J. Geophys. Res., 101, 3139–3156.

Chu, D., & Gordon, R.G., 1998. Current plate motions across the Red Sea. Geophys. J. Inter., 135, 313–328.

Courtillot, V., Jaupart, C., Manighetti, I., Tapponnier, P. & Besse, J., 1999. On causal links between flood basalts and continental breakup. Earth Planet. Sci. Lett., 166, 177–195.

Cox, K.G., Gass, I.G. & Mallick, D.I.J., 1970. The peralkaline volcanic suites of Aden and Little Aden, South Arabia. J. Petrol., 11, 433–461

d'Acremont, E., Leroy, S., Maia, M., Gente, P. & Autin, J. 2010. Volcanism, jump and propagation on the Sheba Ridge, eastern Gulf of Aden: Segmentation evolution and implications for accretion processes. Geophys. J. Int., 180, 535-551.

Davison, I., Al-Kadasi, M., Al-Khirbash, S., Al-Subbary, A.K., Baker, J., Blakey, S., Bosence, D., Dart, C., Heaton, R., McClay, K., Menzies, M., Nichols, G., Owen, L. & Yelland, A., 1994. Geological evolution of the southeastern Red Sea Rift margin, Republic of Yemen. Geo. Soc. Am. Bull., 106, 1474–1493.

Demets, C., Gordon, R.G. & Argus, D.F., 2010. Geologically current plate motions. Geophys. J. Int., 181, 1–80.

Direen, N.G., Stagg, H.M.J., Symonds, P.A. & Colwell J.B., 2008. The architecture of volcanic rifted margins: new insights from the Exmouth-Gascoyne margin, Western Australia. Aust. J. Earth. Sci., 55, 325–347.

Drake C.L. and Girdler R.W., 1964. A geophysical study of the Red Sea. Geophys. J. Roy. Astro. Soc., 8, 473–495.

Dugda, M. T., Nyblade, A. A., Julia, J., Langston, C. A., Ammon, C. J. & Simiyu, S., 2005. Crustal structure in Ethiopia and Kenya from receiver function analysis: Implications for rift development in eastern Africa, J. Geophys. Res., 110, B01303, doi:10.1029/2004JB003065.

Eagles, G., Gloaguen, R. & Ebinger, C., 2002. Kinematics of the Danakil microplate. Earth Planet. Sci. Lett., 203, 607–620.

Ebinger, C.J. & Casey, M. 2001. Continental breakup in magmatic provinces: An Ethiopian example. Geology, 29, 527-530.

Efron, B. & Tibshirani, R., 1986. The Bootstrap Method for standard errors, confidence intervals, and other measures of statistical accuracy. Statistical Sci., 1, No. 1, 1-35.

Egloff, F., Rihm, R., Makris, J., Izzeldin, Y.A., Bobsien, M., Meier, K., Junge, I., Noman, T. & Warsi, W., 1991. Contrasting structural styles of the eastern and westernmargins of the southern Red Sea: the 1988 SONNE experiment. In: J. Makris, P. Mohr and R. Rihm (Editors), Red Sea: Birth and Early History of a New Oceanic Basin. Tectonophysics, 198, 329-353.

El-Anbaawy, M. I. H., Al-Aawah, M. A. H., Al-Thour, K. A. & Tucker, M., 1992. Miocene evaporites of the Red Sea Rift, Yemen Republic: Sedimentology of the Salif halite: Sedimentary Geology, V. 81, P. 61-71.

Fara, M., Chandrasekharam, D., Minissale, A., 1999, Hydrogeochemistry of Damt thermal springs, Yemen Republic: Geothermics, 28, 241–252.

Fournier, M., Patriat P. & Leroy S. 2001. Reappraisal of the Arabia-India-Somalia triple junction kinematics. Earth Planet. Sci. Let., 189, 103-114.

Fournier, M., Chamot-Rooke, N., Petit, C., Huchon, P., Al-Kathiri, A., Audin, L., Beslier, M.O., d'Acremont, E., Fabbri, O., Fleury, J.M., Khanbari, K., Lepvrier, C., Leroy, S., Maillot, B. & Merkouriev, S., 2010. Arabia–Somalia plate kinematics, evolution of the Aden–Owen– Carlsberg triple junction, and opening of the Gulf of Aden. J. Geophys. Res., 115, B04102.

Frederiksen, A.W., Folsom, H. & Zandt, G., 2003. Neighbourhood inversion of teleseismic Ps conversions for anisotropy and layer dip, Geophys. J. Int., 155, 200–212.

Geoffroy, L., Huchon, P. & Khanbari, K., 1998. Did Yemeni tertiary granites intrude neck zones of a stretched continental upper crust? Terra Nova 10, 196–200.

Gernigon, L., Ringenbach, J.C., Planke, S. & Le Gall, B. 2004. Deep structures and breakup along volcanic rifted margins: Insights from integrated studies along the outer Vøring Basin (Norway). Mar. Petrol. Geol., 21, 3, 363-372.

Girdler, R.W. & Styles, P., 1974. Two stage Red Sea floor spreading. Nature, 274, 7-11.

Girdler, R.W. & Underwood, M., 1985. The evolution of early oceanic lithosphere in the southern Red Sea. Tectonophysics, 116, 95-108.

Girdler, R.W., 1991. The case for ocean crust beneath the Red Sea. Tectonophysics, 198 , 275-278.

Gladczenko, T., Hinz, K., Eldholm, O., Meyer, H., Neben, S., & Skogseid, J., 1997. South Atlantic volcanic margins. J. Geol. Soc.-London, 154, 465–470.

Gladczenko, T. P., Skogseid, J. & Eldholm, O., 1998. Namibia volcanic margin. Mar. Geophys. Res.,20,13–341, doi:10.1023/A:1004746101320.

Hammond, J. O. S., Kendall, J.M., Stuart, G. W., Keir, D., Ebinger, C. J., Ayele, A. & Belachew, M., 2011. The nature of the crust beneath the Afar triple junction: Evidence from receiver functions. Geochem. Geophys. Geosyst., 12, doi:10.1029/2011GC003738.

Hansen S.E., Rodgers A.J., Schwartz S.Y. & Al-Amri A.M.S., 2007. Imaging ruptured lithosphere beneath the Red Sea and Arabian Peninsula. Earth Planet. Sci. Lett., 259, 256–265.

Hébert, H., Deplus, C., Huchon, P., Khanbari, K. & Audin, L., 2001. Lithospheric structure of a nascent spreading ridge inferred from gravity data: the western Gulf of Aden. J. Geophys. Res., 106 , 26345–26363

Hughes, G.W. & Beydoun, Z.R., 1992. The Red Sea–Gulf of Aden: biostratigraphy, lithostratigraphy and palaeoenvironments. J. Petrol. Geol., 15, 135–156.

International Seismological Centre, 2012. *On-line Bulletin*, http://www.isc.ac.uk, Internatl. Seis. Cent., Thatcham, United Kingdom.

Jestin, F., Huchon, P. & Gaulier, J.M., 1994. The Somalia plate and the East African Rift System: present kinematics. Geophys. J. Int., 116, 637–654.

Keen, C. E., Dickie, K. & Dehler, S. A., 2012. The volcanic margins of the northern Labrador Sea: Insights to the rifting process. Tectonics, 31, TC1011, doi:10.1029/2011TC002985.

Kennett, B.L.N., & Engdahl, E.R., 1991. Traveltimes for global earthquake location and phase identification. Geophys. J. Int., 122, 429–465.

Kern, H., 1982. Elastic-wave velocity in crustal and mantle rocks at high pressure and temperature: the role of the high-low quartz transition and of dehydration reactions. Phys. Earth Planet. Interiors., 29, 12-23.

Kind, R., et al., , 2002. Seismic images of the crust and upper mantle beneath Tibet: Evidence for Eurasian plate subduction, Science, 298, 1219– 1221.

Langston, C. A., 1977. Corvallis, Oregon, crustal and upper mantle structure from teleseismic P and S waves. Bull. Seism. Soc. Am., 67, 713-724.

Langston, C. A., 1979. Structure under Mount Rainier, Washington, inferred from teleseismic body waves, J. Geophys. Res., 84, 4749-4762.

Laughton, A.S. & Tramontini, C.,.l969. Recent studies of the crustal structure of the Gulf of Aden. Tectonophysics, 8: 359-375.

Leroy, S.,Gente, P., Fournier,M., d'Acremont, E., Patriat, P., Beslier,M.-O., Bellahsen,N.,Maia, M., Blais, A., Perrot, J., Al-Kathiri, A., Merkouriev, S., Fleury, J.-M., Ruellan, P.-Y., Lepvrier, C. & Huchon, P., 2004. From rifting to spreading in the eastern Gulf of Aden: a geophysical survey of a young oceanic basin from margin to margin. Terra Nova 16, 185–192.

Leroy, S., d'Acremont, E., Tiberi, C., Basuyau, C., Autin, J. & Lucazeau, F. 2010a. Recent off-axis volcanism in the eastern Gulf of Aden: implications for plume-ridge interactions. Earth Planet. Sci. Lett., doi:10.1016/j.epsl.2010.02.036, 293, 140-153.

Leroy, S., Lucazeau, F., d'Acremont, E., Watremez, L., Autin, J., Rouzo, S., Bellahsen, N., Tiberi, C., Ebinger, C., Beslier, M.-O., Perrot, J., Razin, P., Rolandone, F., Sloan, H., Stuart, G., Al-Lazki, A., Al-Toubi, K., Bache, F., Bonneville, A., Goutorbe, B., Huchon, P., Unternehr, P. & Khanbari, K. 2010b. Contrasted styles of rifting in the eastern Gulf of Aden: a combined wide-angle MCS and Heat flow survey. Geochem., Geophys., Geosyst. doi:10.1029/2009GC002963.

Leroy, S. et al., 2010c. Continental margins and Ocean-Continent Transitions of the Gulf of Aden: how Africa and Arabia broke up?. Invited speaker. AGU Fall meeting San Francisco.

Leroy S., Razin P., Autin J., Bache F., d'Acremont E., Watremez L., Robinet J., Baurion C., Denèle Y., Bellahsen N., Lucazeau F., Rolandone F., Rouzo S., Serra Kiel J., Robin C. et al.,

2012. From rifting to oceanic spreading in the Gulf of Aden: a synthesis. Arab J. Geosciences. DOI 10.1007/s12517-011-0475-4.

Ligorria, J. & Ammon, G., 1999. Iterative Deconvolution and Receiver Functions Estimation. Bull. Seism. Soc. Am., Vol. 89, 1395-1400.

Ligorria, J.P., 2000. An Investigation of the Crust-Mantle Transition Beneath North America and the Bulk Composition of the North American Crust, Ph.D. Thesis, Saint Louis University, 261 pages.

Lucazeau F., Leroy S., Autin J., Bonneville A., Goutorbe B., Rolandone F., d'Acremont E., Watremez L., Düsünur D. & Huchon P., 2009. Post-rift volcanism and high heat-flow at the ocean–continent transition of the Gulf of Aden. Terra Nova, 21, 285–292.

McKenzie D., 1 978. Some remarks on the development of sedimentary basins. Earth Planet. Sci. Lett. 40, 25-32.

McKenzie, D. P., Davies, D. & Molnar, P., 1970. Plate tectonics of the Red Sea and East Africa. Nature, 226, 243-48.

Makris, J., Henke, C.H., Egloff, F. & Akamaluk, T., 1991. The gravity field of the Red Sea and East Africa. Tectonophysics, 198, 369–382.

Menzies, M.A., Baker, J., Bosence, D., Dart, C., Davidson, I., Hurford, A., Al_Kadasi, M., McClay, K., Nichols, G., Al_Subbary, A. & Yelland, A., 1992. The timing of magmatism, uplift and crustal extension: preliminary observations from Yemen. In: Storey, B.C., Alabaster, T., Pankhurst, R.J. (Eds.), Magmatism and the Causes of Continental Break-up.Special Publication,Vol. 68, 293– 304. Geol. Soc.-London.

Menzies, M.A., Klemperer, S.L., Ebinger, C.J., & Baker, J., 2002, Characteristics of volcanic rifted margins, in Menzies, M.A., Klemperer, S.L., Ebinger, C.J., and Baker, J., eds., Volcanic Rifted Margins: Geological Society of America Special Paper, Vol. 362, 1–14. Boulder, Colorado.

Mjelde, R., Raum, T., Kandilarov, A., Murai, Y. & Takanami, T., 2009. Crustal structure and evolution of the outer Møre Margin, NE Atlantic Tectonophysics, 468, pp. 224–243.

Milkereit B. & Flüh E. R., 1985. Saudi Arabian refraction profile: crustal structure of the Red Sea-Arabian shield transition. Tectonophysics, 111 (1985), pp. 283–299.

Mohr, P. 1991. Structure of Yemeni dike swarms and emplacement of coeval granite plutons. Tectonophysics 198, 203-221.

Mooney, W.D., Gettings, M.E., Blank, H.R. & Healey, J.H., 1985. Saudi Arabian seismic refraction profile: a traveltime interpretation of crustal and upper mantle structure. Tectonophysics 111, 173–246.

Moseley, F., 1969. The Aden traps of Dhala, Musaymir and radfan, South Yemen. Bulletin of Volcanogy, 33, 889–909.

Owens, T. J., Zandt, G. & Taylor, S. R., 1984. Seismic evidence for an ancient rift beneath the Cumberland Plateau, Tennessee: A detailed analysis of broadband teleseismic P-waveforms. J. Geophys. Res., 89, 7783–7795.

Prodehl, C., 1985. Interpretation of a seismic-refraction survey across the Arabian Shield in western Saudi Arabia. Tectonophysics 111, 247–282.

Prodehl, C. & Mechie, J., 1991. Crustal thinning in relationship to the evolution of the Afro-Arabian rift system: a review of seismic-refraction data. In: J. Makris, P. Mohr and R. Rihm(Editors), Red Sea: Birth and Early History of New Oceanic Basin. Tectonophysics, 198, 311-327.

Rey, S.S., Planke, S., Symonds, P. A. & Faleide, J. I. ,2008. Seismic volcanostratigraphy of the Gascoyne margin, western Australia. J. Volcanol. Geotherm. Res., 172, 112–131, doi:10.1016/j.jvolgeores.2006.11.013.

Ruegg, J. C., 1975. Main results about the crustal and upper mantle structure of the Djibouti region (T.F.A.I), in Pilger., A., and Rösler, A., eds., Afar depression of Ethiopia. p. 120-134E. Schweizerbart'sche Verlagsbuchhandlung, Stuttgart.

Sambridge, M,. 1999a. Geophysical inversion with a neighbourhood algorithm-I. Searching a parameter space. Geophys. J. Int., 138, 479–94.

Sambridge, M., 1999b. Geophysical inversion with a neighbourhood algorithm-II. Appraising the ensemble. Geophys. J. Int., 138, 727–46.

Shaw, J. E., Baker, J. A., Ibrahim, K. M. and Menzies, M. A, 2007. The Geochemistry of the Arabian Lithospheric Mantel—a Source for Intraplate Volcanism?.. J. of Petrology 44, 1657-1679

Shibutani, T., Sambridge, M. & Kennett, B., 1996. Genetic algorithm inversion for receiver functions with application to crust and uppermost mantle structure beneath Eastern Australia. Geophys. Res. Lett. 23(14): doi: 10.1029/96GL01671. issn: 0094-8276.

Smith, L.K., White, R.S., & Kusznir, N.J., 2005. Structure of the Hatton Basin and adjacent continental margin. In: Doré AG, Vining BS (eds) Petroleum geology: north-west Europe and global perspectives. Proc 6th Petroleum Geology Conf, 6–9 October 2003, 947–956, Geol. Soc.- London, London.

Stern, R.J., & Johnson, P., 2010. Continental Lithosphere of the Arabian Plate: A Geologic, Petrologic, and Geophysical Synthesis. Earth Sci. Rev., 101, 29-67.

Stuart, G. W., Bastow, I. D. & Ebinger, C. J., 2006. Crustal structure of the northern Main Ethiopian Rift from receiver function studies. In: The Afar Volcanic Province Within the East African Rift System, edited by G. Yirgu, C. J. Ebinger, and P. K. H. Maguire, Geol. Soc. Spec. Publ., 259, 55–72.

Tard, F., Masse, P., Walgenwitz, F. & Gruneisen, P., 1991. The volcanic passive margin in the vicinity of Aden, Yemen. Bulletin Centres Recherche, Exploration–Production Elf-Aquitaine 15, 1–9.

Tiberi, C., Ebinger, C., Ballu, V., Stuart, G., Oluma, B., 2005. Inverse model of gravity data from the Red Sea-Aden-East African rifts triple junction zone, Geophys. J. Int., **163**, doi : 10.1111/j.1365-246X.2005.02736.

Tiberi, C., Leroy, S., d'Acremont, E., Bellahsen, N., Ebinger, C., Al-Lazki, A. & Pointu, A., 2007. Crustal geometry of the northeastern Gulf of Aden passive margin: localization of the deformation inferred from receiver function analysis. Geophys. J. Int., 168(doi:10.1111/j.1365-246X.2006.03294.x): 1247-1260.

Tramontini C. & Davies D., 1969. A seismic Refraction Survey in The Red Sea. Geophys. J.Roy. Astr. Soc., 17, 225–241.

Ukstins, I.A., Renne, P.R., Wolfenden, E., Baker, J., Ayalew, D. & Menzies, M., 2002. Matching conjugate volcanic rifted margins: 40Ar/39Ar chrono-stratigraphy of pre- and syn-rift bimodal flood volcanism in Ethiopia and Yemen. Earth Planet. Sci. Lett., 198, 289–306.

Watanabe, T., 1993. Effects of water and melt on seismic velocities and their application to characterization of seismic reflectors. Geophys. Res. Lett. 20 (2), 933–936.

Watremez, L., Leroy, S., Rouzo, S., d'Acremont, E., Unternehr, P., Ebinger, C., Lucazeau, F., & Al Lazki, A., 2011. The crustal structure of the northeastern Gulf of Aden continental margin: insights from wide-angle seismic data. Geophys. J. Int. 184, 575-594.

White, R.S., Smith, L.K., Roberts, A.W., Christie, P.A.F., Kusznir, N.J., Team, i, 2008. Lower crustal intrusion on the North Atlantic continental margin. Nature 452 (7186), 460–464.

Wolfenden, E., Ebinger, C., Yirgu, G., Renne, P. & Kelley, S.P. 2005. Evolution of the southern Red Sea rift: birth of a magmatic margin. Geol. Soc. Am. Bull., 117, 846-864.

Zandt, G. & Ammon, C.J., 1995. Continental crust composition constrained by measurement of crustal Poisson's ratio. Nature 374, 152–154.

Zhu, L., 2000. Crustal structure across the San Andreas Fault, Southern California from teleseismic converted waves: Earth Planet. Sci. Lett., 179, 183-190.

Zhu, L. & Kanamori, H., 2000. Moho Depth Variation in Southern California from Teleseimic Receiver Function. J.Geophys. Res., 105, 2969-2980.

Table and Figure Captions

Table1. Crustal thickness (H) and Vp/Vs ratio results for seismic stations of western profile - western Yemen. The average crustal velocity used is 6.2 km/s for all of the plateaue and most of the coastal plain stations, except UAYA and ZUWA(SW) where 5.3 km/s is used. The average crustal velocity is derived from Egloff et al 1991.

Figure 1. Land-sat imagery and Sea-sat bathymetry showing the seismicity along the boundaries between Arabian plate and adjacent areas. The seismic data are extracted from ISC seismic catalogue for the period Jan., 1970 – Feb., 2012 and M≥5.0 (International Seismological Centre , 2012). AFFZ is Alula-Fartaq fracture zone. The large black arrows are pointing to the direction of motion of different plates in the region.

Figure 2. a) Geological map of the study area showing different geological units (modified from Geological Survey and Mineral Resources Board - Yemen), with the seismic stations location for the western area of YOCMAL project and stations from Yemen permanent seismic network. The thick black line shows the location of the SONNE 1988 seismic profile. b) Backazimuth events distribution of the events on a projection centred on the North Pole. Circles are every 10º of distance.

Figure 3. Stacked receiver functions for 16 seismic stations of our study: a) for north-south section of the profile, b) for the east-west section, c) Stations along Red Sea coast, d) stations parallel to Gulf of Aden. The arrows represent the arrival of the

Moho Ps (black), PpPs (red) and PpSs+PsPs (blue) phases from the Moho. See inset in e for explanation of the Moho Ps and the multiple phases crustal paths.

Figure 4. Receiver functions for 6 stations of the profile. The receiver functions are organized by increasing backazimuth (red number right of the trace). The light vertical lines indicate arrival times for conversion phases (Ps and multiples) from the Moho for the maximum stacking amplitude.

Figure 5. Thickness (H) versus Vp/Vs ratio diagrams from the H-k stacking method for 6 of our stations in figure 4. The maximum of the stacking amplitude is indicated by the white point and corresponds to the value indicated in Tab. 1. The scale bar is the amplitude of stacking function.

Figure 6. RF and cross-section western Gulf of Aden volcanic margin. a) cross section showing Moho depth and high velocity lower crust (HVLC) from our results and the interpretation of seismic line after Tard *et al.,* 1991. b) RF of ADEN station with vertical lines showing the Moho conversion phase and multiples. c) Crustal thickness H versus Vp/Vs ratios, scale bar is the amplitude of the stacking function, white star is the maximum of the H-k plot, red arrow pointing to the Moho depth and blue arrow showing the depth of HVLC. d) RF with vertical lines showing HVLC conversion phase and multiples. The RF's are annotated by red numbers (backazimuth).

Figure 7. Left: Seismic velocity models for RUSA and DKUM stations obtained from the neighbourhood algorithm method (Sambridge, 1999a). The grey area indicates all the models searched by the algorithm. The best 1000 models are indicated in

yellow-green colour, the best one (smallest misfit) corresponds to the red line, both for S-wave velocity and Vp/Vs ratio and the white line is the average velocity model. Right: waveform matches between the observed stacked receiver functions (green) and the predicted one (red) based on the best models (red lines in the left-hand diagrams).

Figure 8. Neighbourhood algorithm (NA) inversion and direct modelling results for ADBA. a) Velocity models explored with the NA inversion. The best model is indicated with the red line and corresponds to the red receiver function signal in (b). c) Velocity model used to obtain the dark blue modelled receiver function in (d).

Figure 9. Receiver Function (RF) and cross-section across the Red Sea volcanic Margin. a) Cross section of Moho discontinuity and the high velocity lower crust (HVLC), with the projection of seismic line after Davison *et al.,* 1994. b) RF and H versus Vp/Vs ratio diagrams from H-k stacking results for UAYA station. Vertical lines show the Moho conversion phase and multiples top and HVLC conversion phase with multiples bottom. c) RF and H versus Vp/Vs diagrams for ZUWA station. Top, ZUWA RF organized by increasing backazimuth as indicated by red numbers to the right. Middle, RF for backazimuth range $>140^0$ and bottom, RF for backazimuth$<106^0$. Crustal thickness, Vp/Vs ratio and average crustal Vp used for inversion are marked by blue text in the RF figures.

Figure 10. Migrated cross-sections following the main profile sections, E-W (bottom centered at MAWI oriented N100E) and N-S (top centered at DAMT oriented NS). The Moho depth estimated from H-k stacking method is plotted with the black dots

with error bars from bootstrap. Red colour indicates velocity increase with depth, and blue colour velocity decrease with depth. Scale bar shows amplitude of positive (red) and negative (blue) polarities of arrivals.

Figure 11. Regional map showing Moho depths (below sea level) based on the results of this study (red triangles) and previous RF studies (black triangles) in Ethiopia (Hammond *et al.,* 2011), and Saudi Arabia (Hansen *et al.,* 2007), active seismic studies (black dots) in the Red Sea (Egloff. *et al.,* 1991, Tramontini & Davies, 1969; Drake & Girdler, 1964), controlled source study in the Western Gulf of Aden (Laughton & Tramontini, 1969), seismic refraction profiles in Djibouti (Ruegg, 1975) and Saudi Arabian seismic refraction profile (Mooney et al., 1985).

Table1

Location	Station name	Number of RF	Latitude (N)	Longitude (E)	Elevation (m)	Crustal thickness (km)	Vp/Vs Ratio	Error in depth (km)	Error In Vp/Vs	Poisson's Ratio (σ)
S to N Section	ADEN	45	12.77592	44.98244	59	20.4	1.73	2.08	0.057	0.25
	DKUM	19	13.27108	44.75736	397	23.6	1.69	0.37	0.030	0.23
	ADBA	36	13.55078	44.84239	705	31	1.68	1.78	0.053	0.23
	KHLA	21	13.79685	44.80798	1457	33.8	1.75	5.99	0.090	0.26
	DAMT	35	14.08737	44.68227	1902	35.2	1.83	0.42	0.017	0.29
	DAMY	30	14.57133	44.39000	2460	35.2	1.79	2.28	0.051	0.27
	RUSA	29	14.70738	44.35394	2332	35.2	1.76	1.49	0.035	0.26
	YSLE	43	14.93873	44.28157	2557	35.0	1.77	0.49	0.020	0.27
	SANA	34	15.39263	44.20682	2253	35.4	1.78	1.32	0.034	0.27
E to W section	SHIB	33	15.50305	43.90550	2630	35.8	1.80	2.76	0.056	0.28
	TAWI	26	15.47866	43.72389	2333	32.2	1.79	1.99	0.049	0.27
	MAWI	36	15.46748	43.52317	1875	31.4	1.74	2.98	0.064	0.25
	ANID	23	15.47365	43.20478	147	22.8	1.83	0.46	0.031	0.29
	ZUWA	27	15.72752	43.02184	87	23.0	1.91	1.95	0.057	0.31
	UAYA	28	15.70929	42.69337	9	13.8	1.92	0.26	0.027	0.31
Along Red Sea	SUGH	10	14.79705	43.44282	248	23.2	1.73	2.17	0.044	0.25
	KHAW	30	13.80802	43.25408	14	23.0	1.68	0.34	0.138	0.23
	MOKA	25	13.31374	43.25631	29	21.5	1.85	3.35	0.061	0.29
Parallel to Gulf of Aden	TRBA	77	13.231	44.116	1860	27.4	1.86	1.37	0.054	0.30
	LBOS	49	13.871	45.250	2325	32.6	1.83	0.53	0.018	0.29
	BDHA	29	13.975	45.567	2000	36.2	1.76	0.62	0.029	0.26

Fig.(1)colour

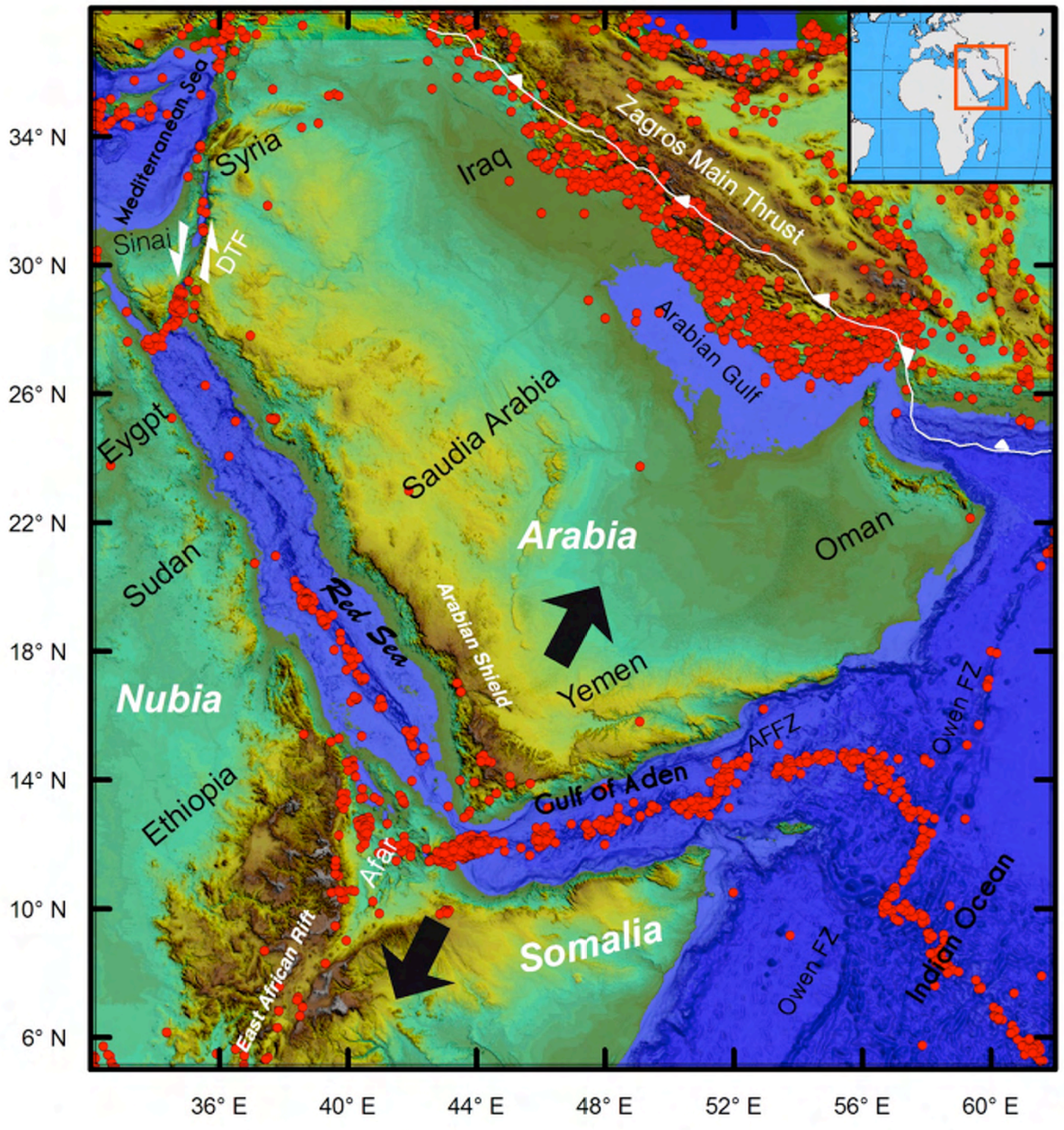
Mediterranean Sea
Syria
Iraq
Zagros Main Thrust
Sinai
DTF
Arabian Gulf
Eygpt
Saudia Arabia
Arabia
Oman
Sudan
Red Sea
Arabian Shield
Yemen
Nubia
AFFZ
Owen FZ
Ethiopia
Gulf of Aden
Afar
Somalia
East African Rift
Owen FZ
Indian Ocean
34° N
30° N
26° N
22° N
18° N
14° N
10° N
6° N
36° E
40° E
44° E
48° E
52° E
56° E
60° E

Fig.(2) Colour

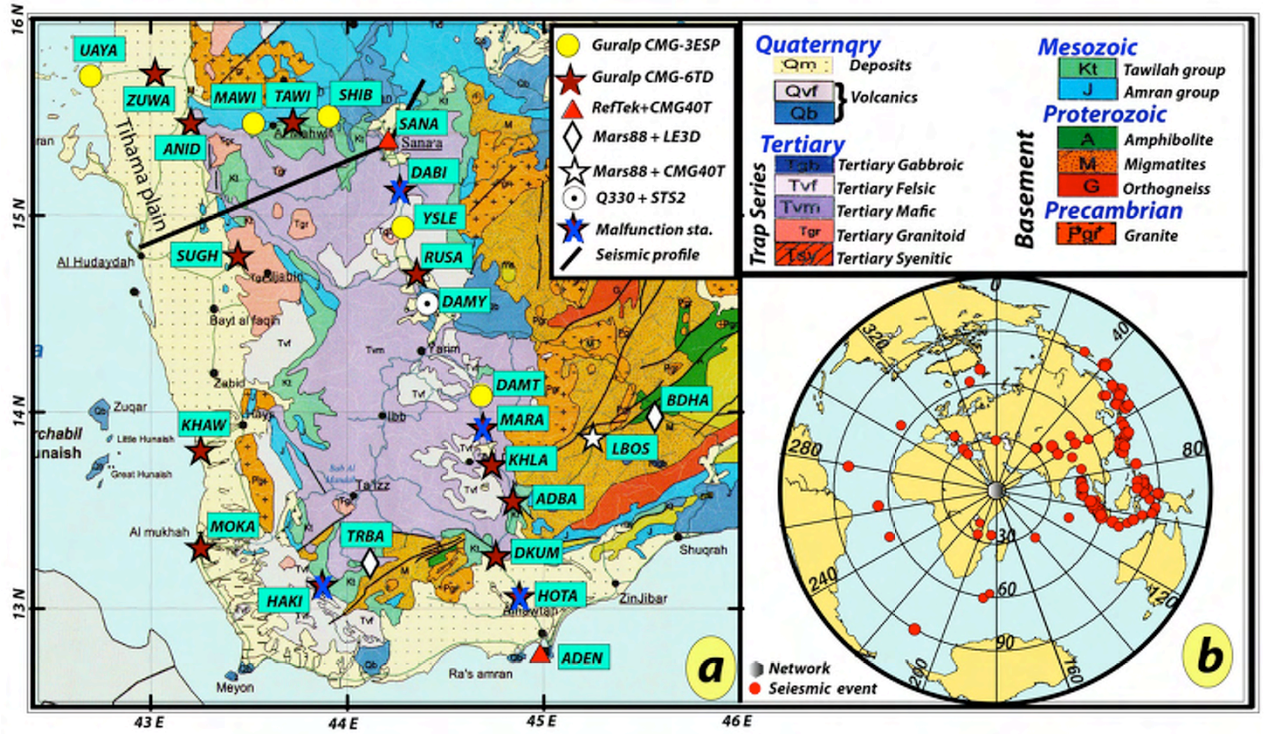
UAYA
ZUWA
MAWI
TAWI
SHIB
SANA
Sana'a
ANID
DABI
YSLE
SUGH
RUSA
DAMY
DAMT
MARA
KHLA
ADBA
BDHA
LBOS
KHAW
MOKA
TRBA
DKUM
HAKI
HOTA
ADEN
Tihama plain
Al Hudaydah
Bayt al faqih
Zabid
Zuqar
Little Hunaish
Great Hunaish
Al mukhah
Ta'izz
Shuqrah
ZinJibar
Ra's amran
Meyon
16 N
15 N
14 N
13 N
43 E
44 E
45 E
46 E
Guralp CMG-3ESP
Guralp CMG-6TD
RefTek+CMG40T
Mars88 + LE3D
Mars88 + CMG40T
Q330 + STS2
Malfunction sta.
Seismic profile
Quaternary
Qm Deposits
Qvf Volcanics
Qb
Tertiary
Tgb Tertiary Gabbroic
Tvf Tertiary Felsic
Tvm Tertiary Mafic
Tgr Tertiary Granitoid
Tsy Tertiary Syenitic
Trap Series
Mesozoic
Kt Tawilah group
J Amran group
Proterozoic
A Amphibolite
M Migmatites
G Orthogneiss
Precambrian
Pgr Granite
Basement
a
b
Network
Seismic event

Fig.(3) Colour

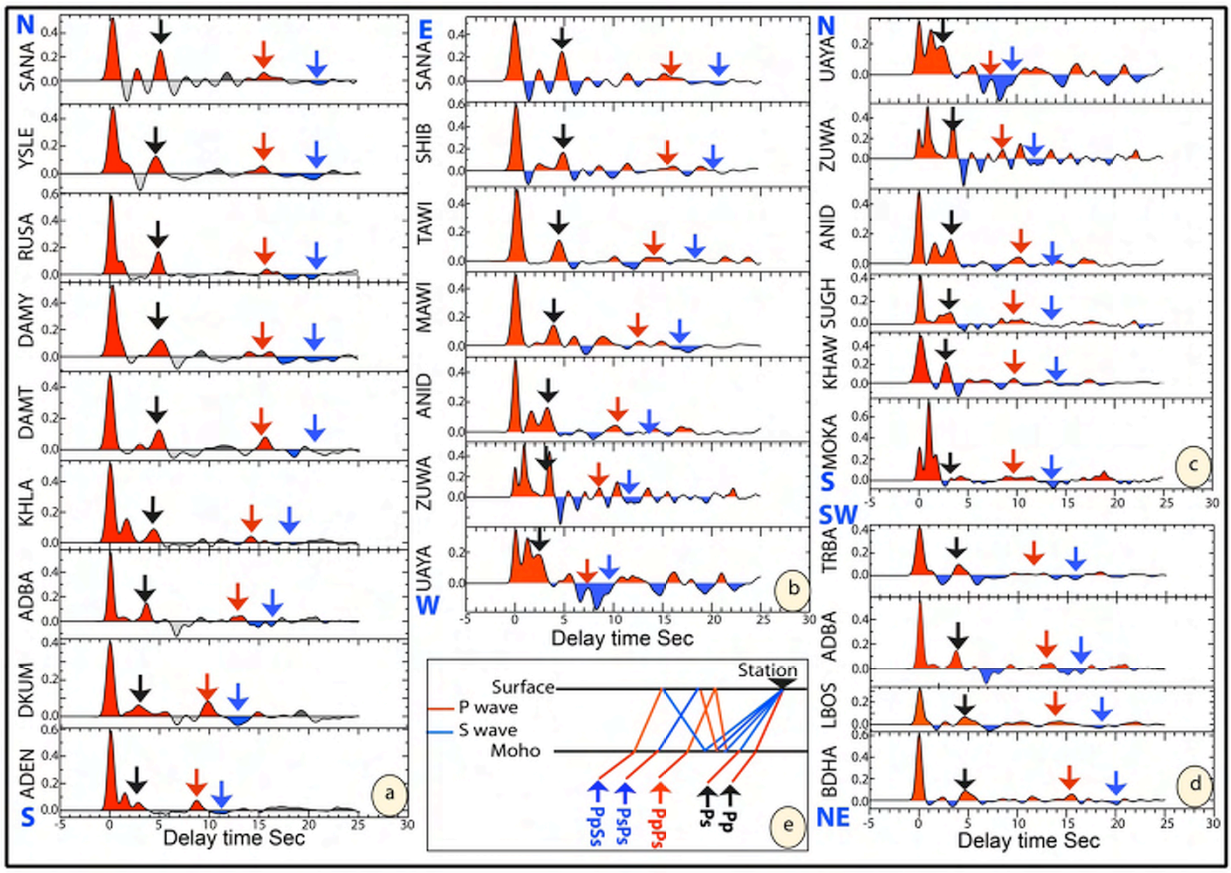
N
S
E
W
N
SW
NE
SANA
YSLE
RUSA
DAMY
DAMT
KHLA
ADBA
DKUM
ADEN
SHIB
TAWI
MAWI
ANID
ZUWA
UAYA
ZUWA
ANID
SUGH
KHAW
MOKA
TRBA
ADBA
LBOS
BDHA
a
b
c
d
e
Delay time Sec
Surface
P wave
S wave
Moho
Station
PpSs
PsPs
PpPs
Ps
Pp

Fig.(4) Colour

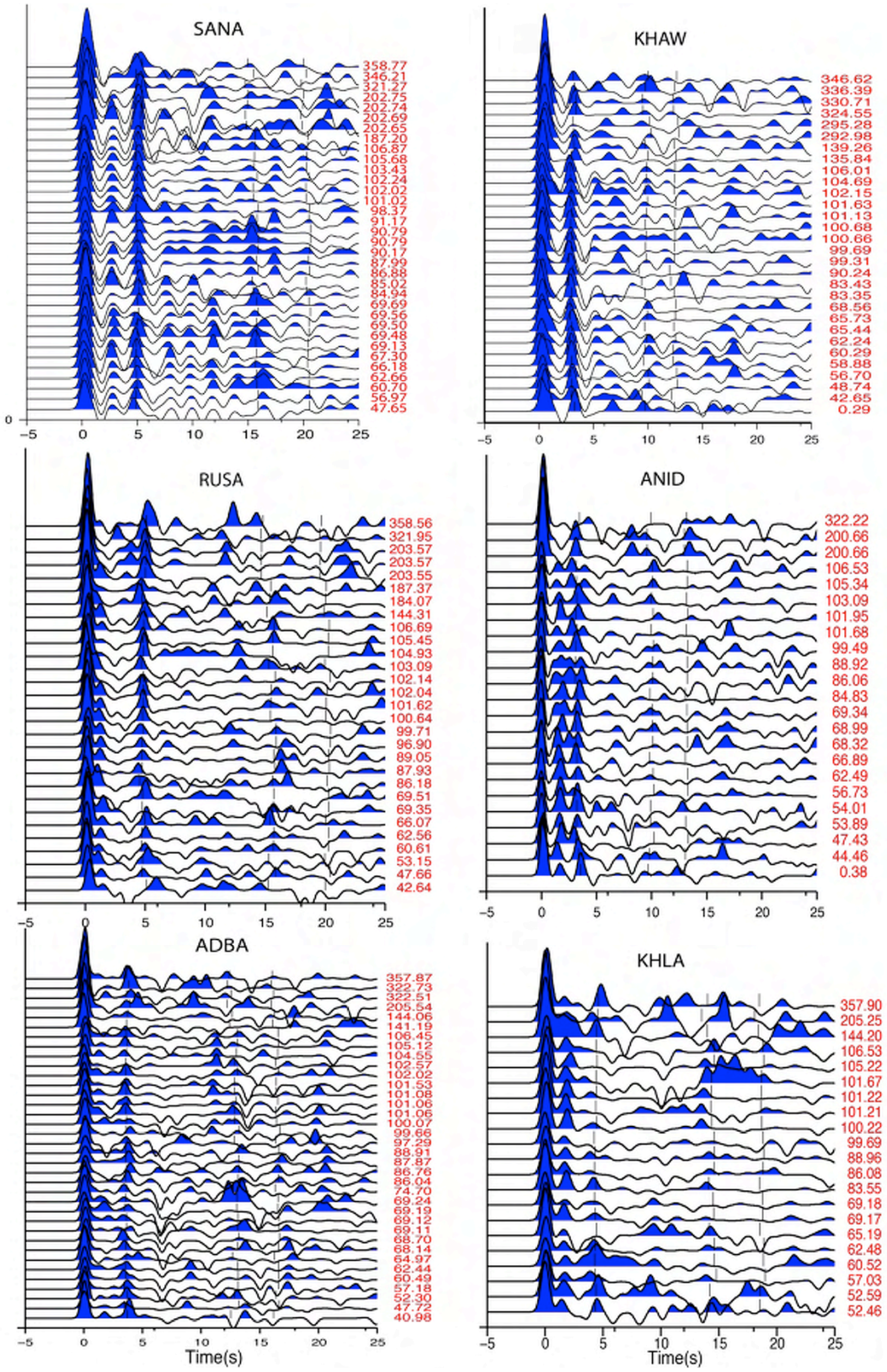
SANA
358.77
346.21
321.27
202.75
202.74
202.69
202.65
187.20
106.87
105.68
103.43
102.24
102.02
101.02
98.37
91.17
90.79
90.79
90.17
87.99
86.88
85.02
84.94
69.69
69.56
69.50
69.48
69.13
67.30
66.18
62.66
60.70
56.97
47.65
0
−5 0 5 10 15 20 25
KHAW
346.62
336.39
330.71
324.55
295.28
292.98
139.26
135.84
106.01
104.69
102.15
101.63
101.13
100.68
100.66
99.69
99.31
90.24
83.43
83.35
68.56
65.73
65.44
62.24
60.29
58.88
56.70
48.74
42.65
0.29
−5 0 5 10 15 20 25
RUSA
358.56
321.95
203.57
203.57
203.55
187.37
184.07
144.31
106.69
105.45
104.93
103.09
102.14
102.04
101.62
100.64
99.71
96.90
89.05
87.93
86.18
69.51
69.35
66.07
62.56
60.61
53.15
47.66
42.64
−5 0 5 10 15 20 25
ANID
322.22
200.66
200.66
106.53
105.34
103.09
101.95
101.68
99.49
88.92
86.06
84.83
69.34
68.99
68.32
66.89
62.49
56.73
54.01
53.89
47.43
44.46
0.38
−5 0 5 10 15 20 25
ADBA
357.87
322.73
322.51
205.54
144.06
141.19
106.45
105.12
104.55
102.57
102.02
101.53
101.08
101.06
101.06
100.07
99.66
97.29
88.91
87.87
86.76
86.04
74.70
69.24
69.19
69.12
69.11
68.70
68.14
64.97
62.44
60.49
57.18
52.30
47.72
40.98
−5 0 5 10 15 20 25
Time(s)
KHLA
357.90
205.25
144.20
106.53
105.22
101.67
101.22
101.21
100.22
99.69
88.96
86.08
83.55
69.18
69.17
65.19
62.48
60.52
57.03
52.59
52.46
−5 0 5 10 15 20 25
Time(s)

Fig.(5) Colour

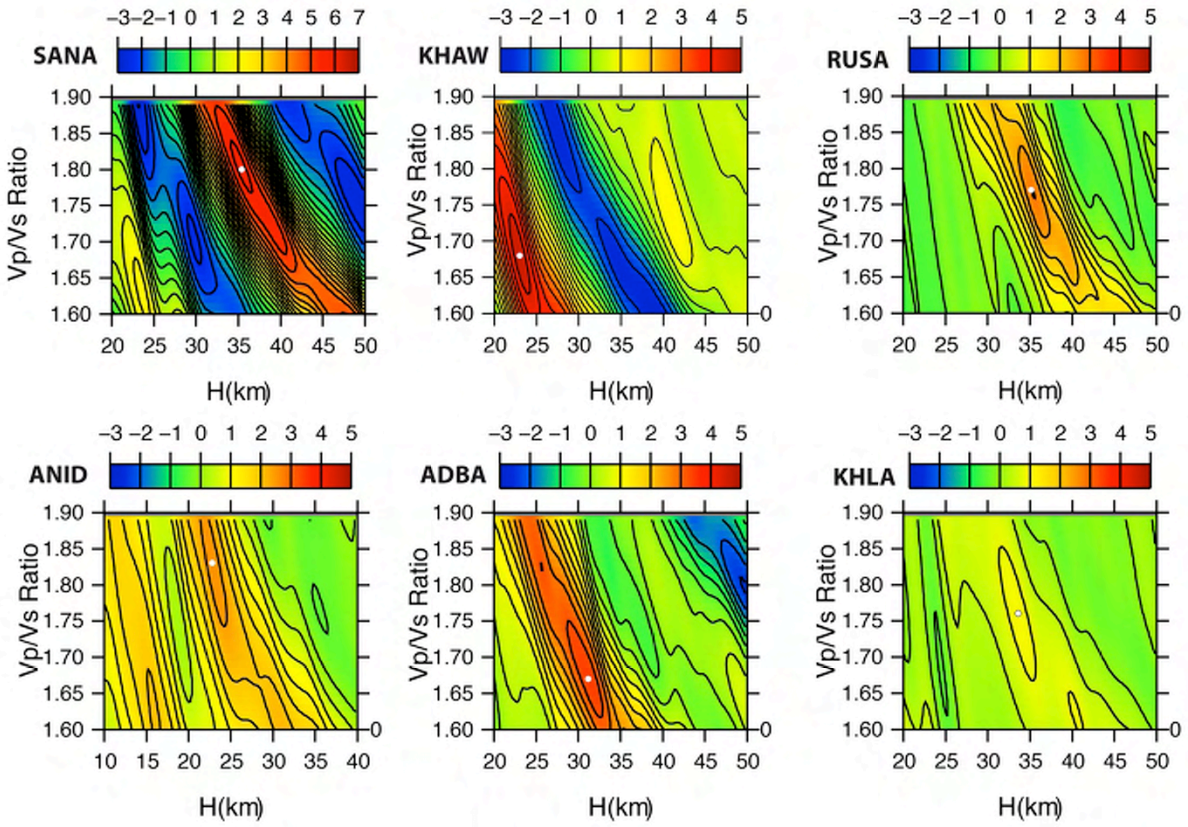

Fig.(6) Colour

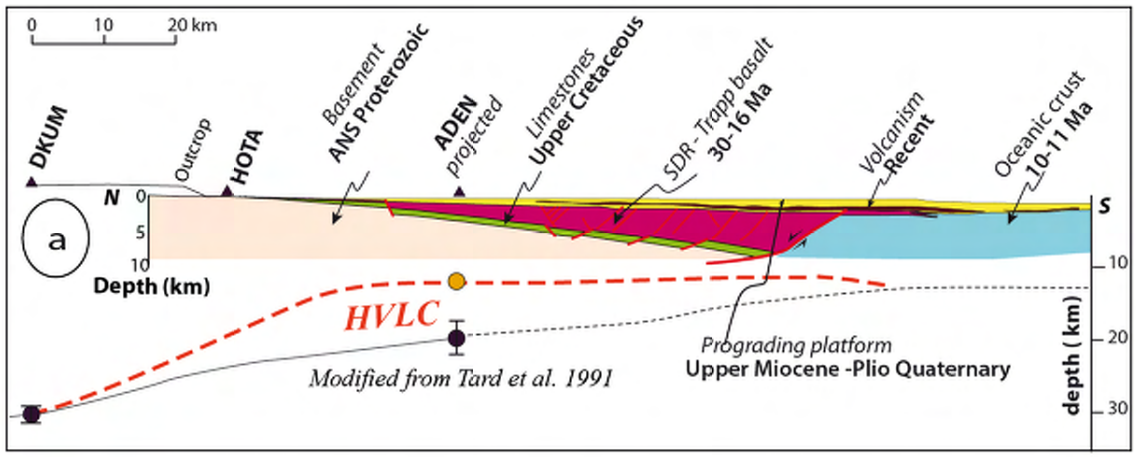
0 10 20 km
DKUM
Outcrop
HOTA
Basement
ANS Proterozoic
ADEN
projected
Limestones
Upper Cretaceous
SDR - Trapp basalt
30-16 Ma
Volcanism
Recent
Oceanic crust
10-11 Ma
N
S
a
Depth (km)
HVLC
Modified from Tard et al. 1991
Prograding platform
Upper Miocene -Plio Quaternary
depth (km)

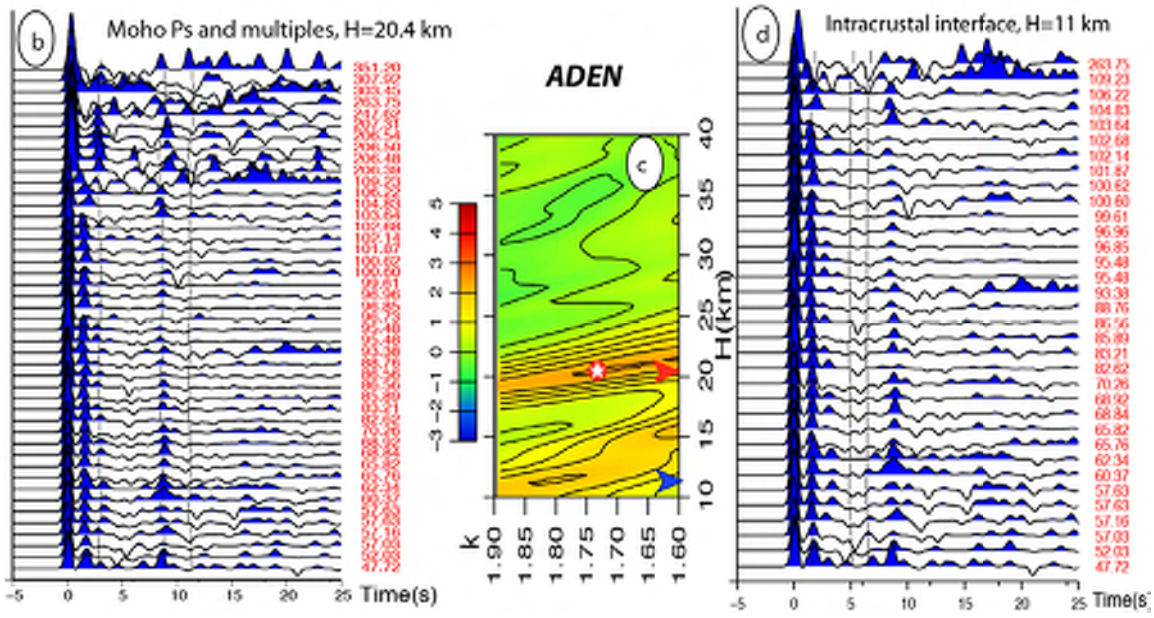
b
Moho Ps and multiples, H=20.4 km
Time(s)
ADEN
c
k
H(km)
d
Intracrustal interface, H=11 km
Time(s)

Fig.(7) Colour

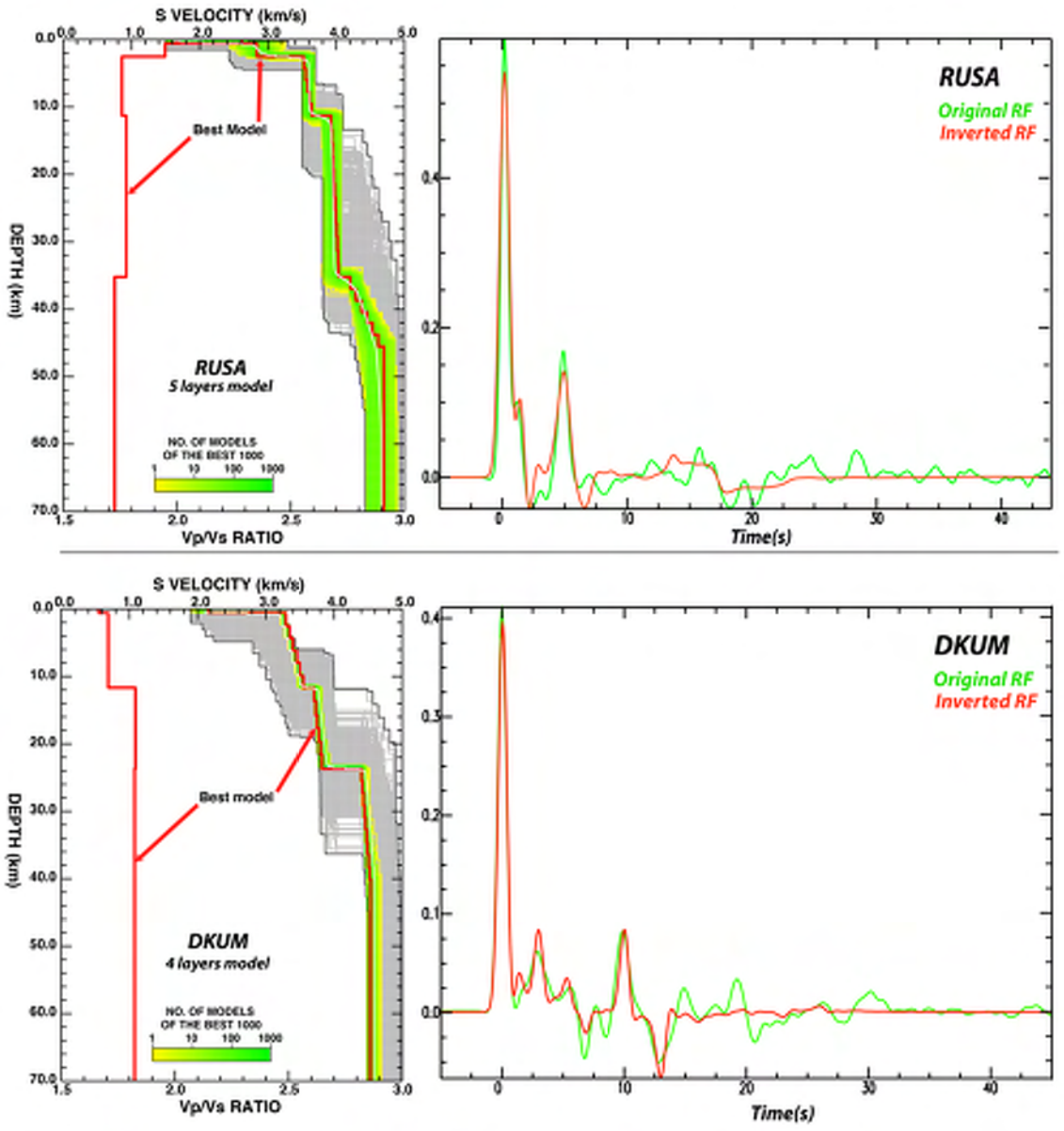
S VELOCITY (km/s)
Best Model
RUSA
5 layers model
NO. OF MODELS OF THE BEST 1000
DEPTH (km)
Vp/Vs RATIO
RUSA
Original RF
Inverted RF
Time(s)
S VELOCITY (km/s)
Best model
DKUM
4 layers model
NO. OF MODELS OF THE BEST 1000
DEPTH (km)
Vp/Vs RATIO
DKUM
Original RF
Inverted RF
Time(s)

Fig.(8) Colour

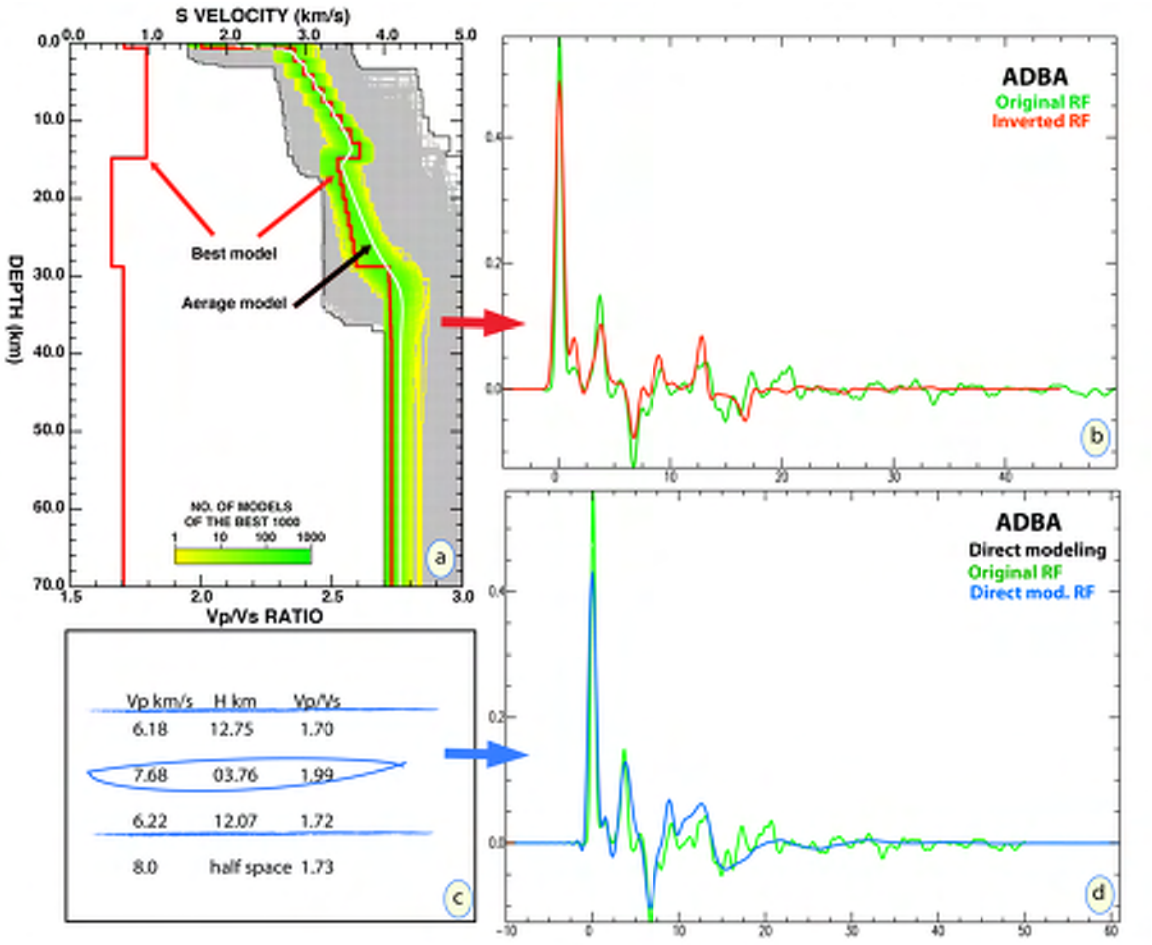
S VELOCITY (km/s)
DEPTH (km)
Best model
Aerage model
NO. OF MODELS OF THE BEST 1000
Vp/Vs RATIO
a
Vp km/s H km Vp/Vs
6.18 12.75 1.70
7.68 03.76 1.99
6.22 12.07 1.72
8.0 half space 1.73
c
ADBA
Original RF
Inverted RF
b
ADBA
Direct modeling
Original RF
Direct mod. RF
d

Fig.(9) Colour

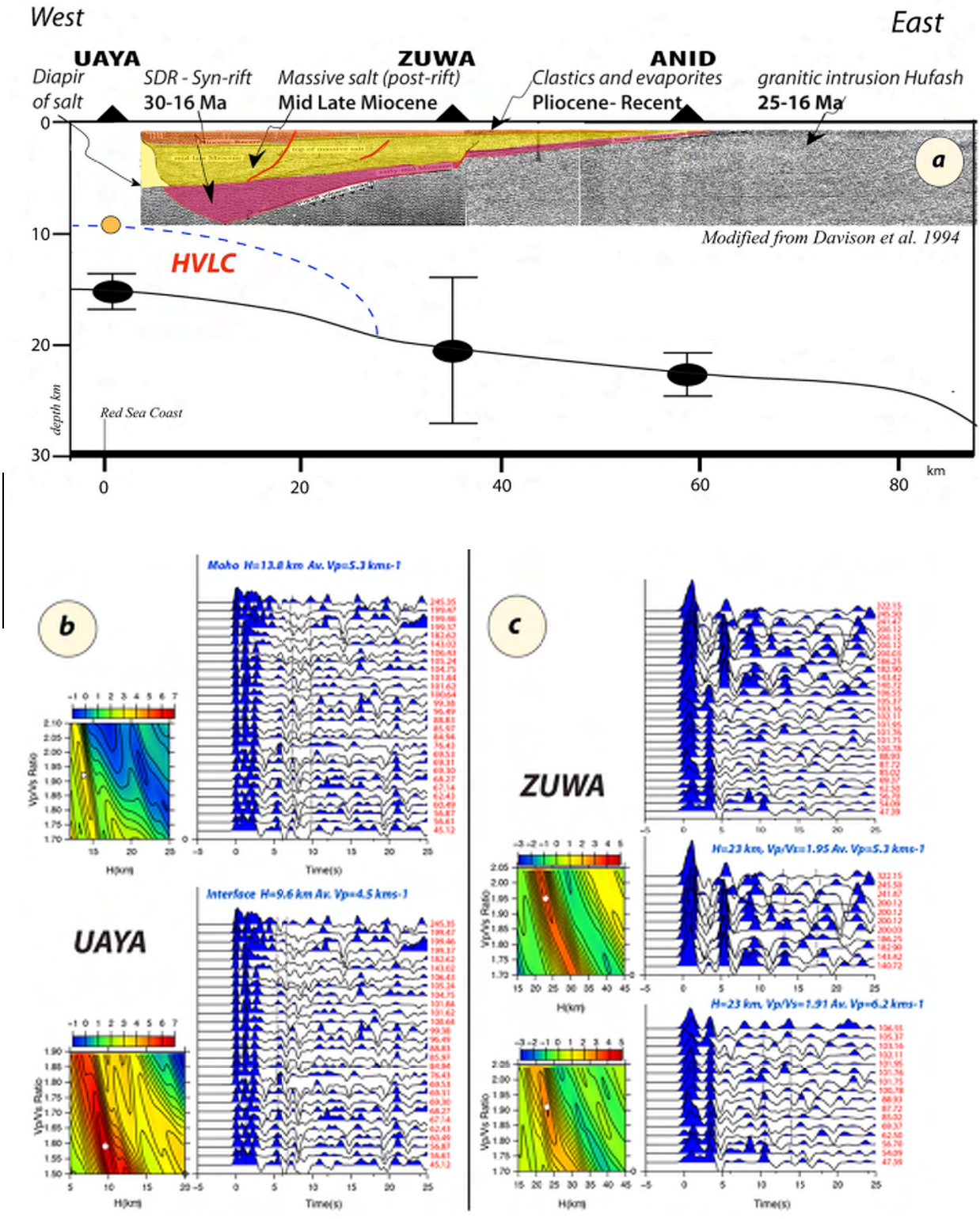
West
East
UAYA
ZUWA
ANID
Diapir of salt
SDR - Syn-rift 30-16 Ma
Massive salt (post-rift) Mid Late Miocene
Clastics and evaporites Pliocene- Recent
granitic intrusion Hufash 25-16 Ma
a
Modified from Davison et al. 1994
HVLC
depth km
Red Sea Coast
km
b
Moho H=13.8 km Av. Vp=5.3 kms-1
Interface H=9.6 km Av. Vp=4.5 kms-1
UAYA
Vp/Vs Ratio
H(km)
Time(s)
c
ZUWA
H=23 km, Vp/Vs=1.95 Av. Vp=5.3 kms-1
H=23 km, Vp/Vs=1.91 Av. Vp=6.2 kms-1

Fig.(10) Colour

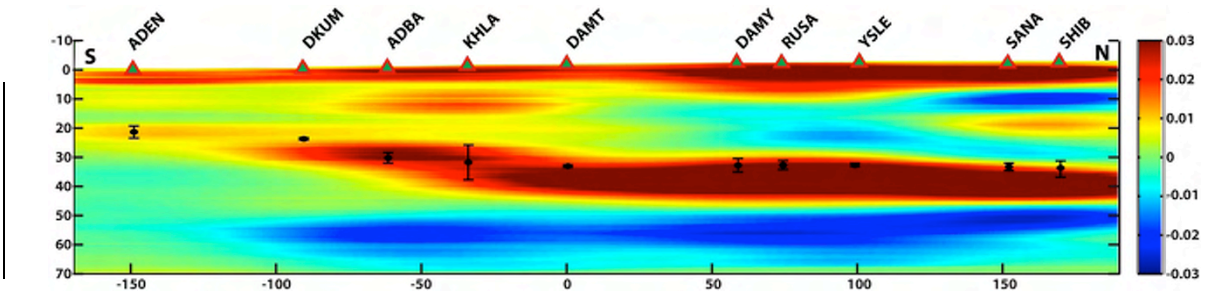

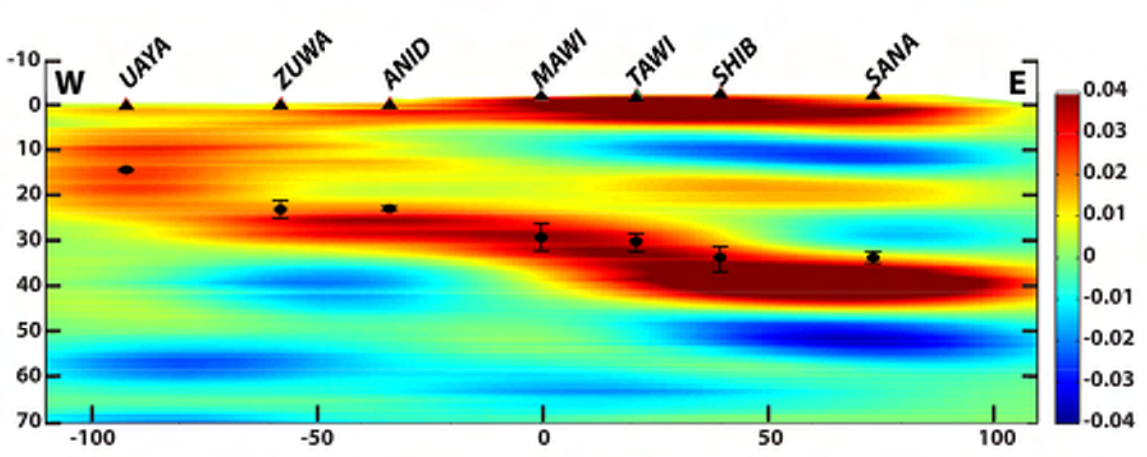

Figure (11) Colour

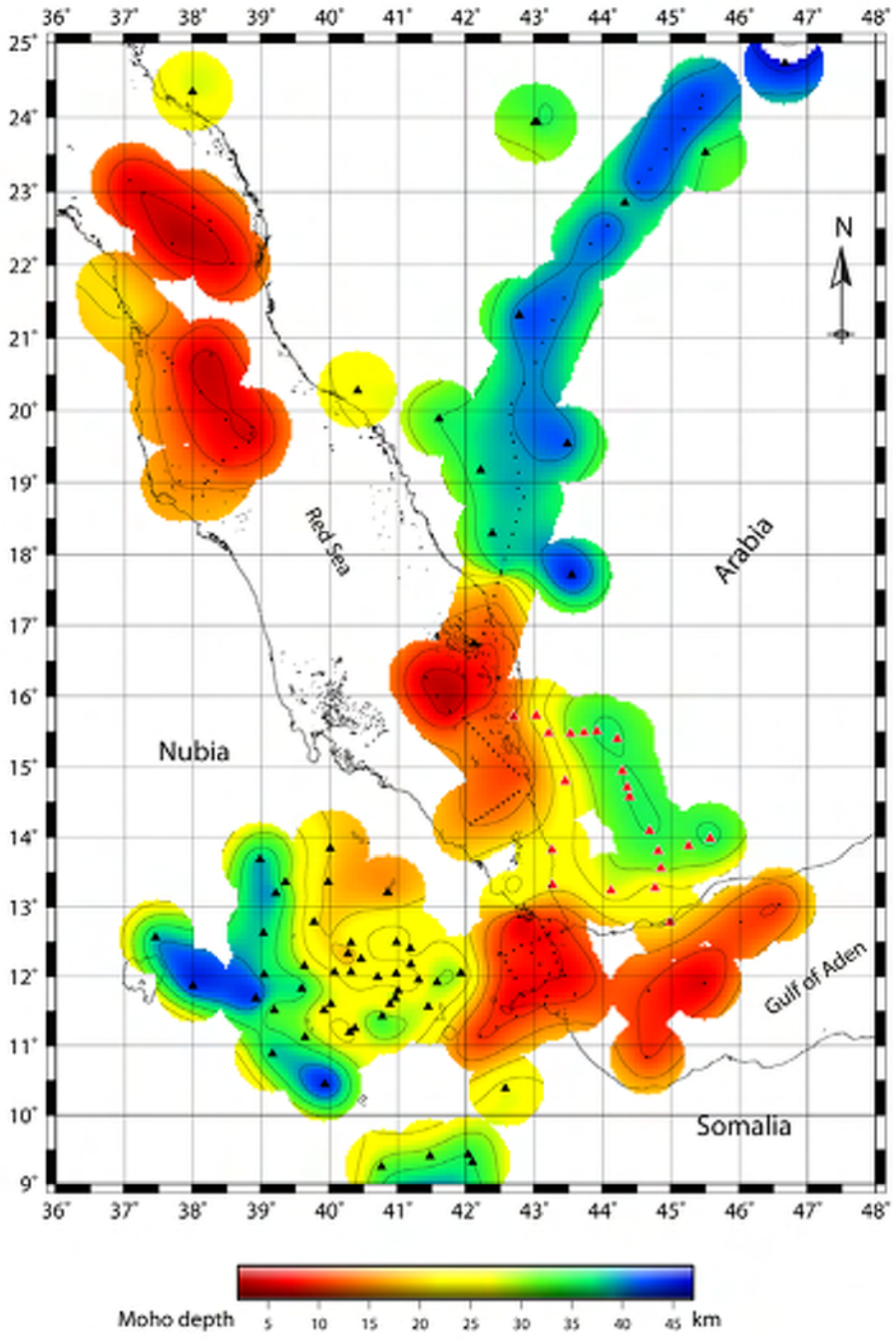
36° 37° 38° 39° 40° 41° 42° 43° 44° 45° 46° 47° 48°
25° 24° 23° 22° 21° 20° 19° 18° 17° 16° 15° 14° 13° 12° 11° 10° 9°
N
Red Sea
Arabia
Nubia
Gulf of Aden
Somalia
Moho depth
5 10 15 20 25 30 35 40 45 km

Supplemental material for:

Crustal structure of the rifted volcanic margins and uplifted plateau of Western Yemen from receiver function analysis

Ahmed, A., Tiberi, C., Leroy, S., Stuart, G.,Keir, D. , Sholan, J., Khanbari, K., Al-Ganad I., Basuyau, C.

This material provides supplemental figures and plots of the receiver function for 12 stations, velocity-depth inversion results at two stations and statistical error estimates for all stations.

Receiver function analysis

We constrain our data selection to events with magnitude > 5.5, within epicentral distance in the range 25^0 (to have more events to the south, west and northwest) to 95^0. For each station-event pair, 30s window is analysed (5 sec before the P onset time 25s after) and the receiver function is calculated using the time-domain iterative deconvolution method (Ammon, 1991). We retain those receiver functions where the final deconvolution reproduces > 75% of the signal. A visual quality-check inspection of the receiver functions was then undertaken to remove further low-quality receiver functions.

We apply Zhu and Kanamori (2000) to estimate the thickness H and the Vp/Vs ratio of the crust. The results of our inversion at 9 stations are shown in the main text and in this supplementary material we show the results at the other 12 stations. Figure

S1 displays the individual receiver functions at each station and figure S2 the associated inverted crustal thicknesses and Vp/Vs ratios.

Waveform modeling and shear wave velocity inversion

As mentioned in the text, for those stations with complex signal the stochastic waveform method (Shibutani et al., 1996) is used to invert our receiver functions to 1D velocity depth models using the Neighbourhood Algorithm technique (Sambridge, 1999a, 1999b).

Here we provide the waveform modeling and shear wave velocity results for two stations of the coastal plain near the Red Sea. As mentioned in the text the receiver functions at ZUWA and MOKA are very complex with at least two intracrustal conversion phases in a short time window after the onset of P wave. The first one with strong dependency on the backazimuth arrives in 1 to 2 sec after the onset of the P wave and characterized by higher amplitude than the first arrival. We interpret this conversion phase to have occurred between the sedimentary cover (Vp/Vs > 2) and underlying higher velocity layer. The initial model consisted of 5 layers: sedimentary cover, basement, upper and lower crust over a mantle half space.

The receiver functions at ZUWA (N-E) and MOKA are successfully modeled and the results are comparable to the initial velocity model for ZUWA (N-E) but are slightly different to MOKA as the lower crust is of higher velocity. For ZUWA (S-W) the high amplitude intracrustal phase arriving 1-1.5 sec after the P onset and high amplitude Moho conversion phase Ps, are very difficult to model using this method or any

other forward modeling technique. However, the best fit model for this waveform (Fig. S3) in terms of the arrival time of the converted phases, is obtained using Shibutani method with initial velocity model consisting of a 4 km thick sedimentary cover with Vp ranging between 1.8-3.9 km/s (Egloff et al., 1991) underlain by 19 km thick crust with an average velocity of 5.9 km/s. All the inversion results are as shown in figure S3 of this supplementary material.

Stability of the results

The stability of the H-*k* inverted results using the receiver function method is strongly dependent on the clarity of the phases on the receiver function waveforms and backazimuth coherency of the Moho converted phase *Ps* and multiples (*PpPs* and *PpSs+PsPs*). The crustal thickness determined is affected by the average crustal velocity assumed to perform the inversion.

First, due to the lack of a *priori* velocity information we tested the H-*k* technique with a range of average crustal velocities Vp (5.8, 6.0, 6.2, 6.4, 6.6 and 6.8 km/s) to estimate the appropriate average velocity which could be used in the inversion for H and *k* and represent different regions on the plateau and coastal areas (an example of the results is shown in fig. S5-a). We chose to use 6.2 km/s to perform our presented results so that they could be compared to the results of the previous work in similar tectonic settings (Al-Damegh et al., 2005; Tiberi et al., 2007 and Hammond et al., 2011). Second, we implement a robust bootstrap statistical technique (Efron & Tibshirani, 1991), to estimate the uncertainties and the stability of our results such

that the Zhu & Kanamori (2000) stacking method is used to calculate H and k for 200 randomly generated data subsets of the original RF's. The standard deviations for H and k are estimated from the covariance matrix (Tiberi et al., 2007).

Finally the variations in the crustal thickness and Vp/Vs ratio coming from the inversion method (plain lines ellipses) are greater than the uncertainty coming from the initial velocity model (dashed lines ellipses) (Fig. S5 b-d). It also illustrates that the error estimates of our results have a strong backazimuth dependency. ADEN, KHLA and MOKA stations illustrate this effect (Fig. S5b-S5d); the amplitude and/or coherency of the Moho conversion phase Ps and multiples vary significantly with back azimuth.

Figure S1

Receiver functions for 12 stations of the profile. The receiver functions are organized by increasing backazimuth (red number right of the trace). The light vertical lines indicate arrival times for conversion phases (Ps and multiples) from the Moho for the maximum stacking amplitude.

Figure S2.

Thickness (H) versus Vp/Vs ratio diagrams from the H-k stacking method for the 12 stacked receiver functions shown in Figure S1. The maximum of the stacking amplitude is indicated by the white point and corresponds to the value indicated in Tab. 1.

Figure S3

Left: Seismic velocity models for MOKA station obtained from the neighbourhood algorithm method (Sambridge, 1999a). The best 1000 models are indicated in yellow-green colour, and the best one (smallest misfit) corresponds to the red line, both for S-wave velocity and Vp/Vs ratio. Right: waveform matches between the observed stacked receiver functions (green) and the predicted one (red) based on the best models (red lines in the left-hand diagrams). The white and blue lines in the left-hand diagram are the reference models of the velocity and Vp/Vs ratio, respectively.

Figure S4.

a) Left: Seismic velocity models for NE of ZUWA station obtained from the neighbourhood algorithm method (Sambridge, 1999a). The best 1000 models are indicated in yellow-green colour, and the best one (smallest misfit) corresponds to the red line, both for S-wave velocity and Vp/Vs ratio. Right: waveform matches between the observed stacked receiver functions (green) and the predicted one (red) based on the best models (red lines in the left-hand diagrams). The white and blue lines in the left-hand diagram are the reference models of the velocity and Vp/Vs ratio, respectively.

b) Forward modelling of the ZUWA receiver functions for backazimuth > 140^{o}, signal black is the original RF and red is the generated RF using the velocity model at the upper right corner.

Figure S5

An example of the inverted H-k values using different average crustal velocity Vp in the range 5.8 - 6.8 km/s is shown in (a).

Vp/Vs as a function of crustal thickness H with bootstrap error estimates for the stacking method in plain lines and in dashed lines coming from the initial velocity model for the NS section of the profile in (b), EW section of the profile in (c) and stations parallel to the Red Sea, south and east of plateau in (d). Three distinct error estimates were determined for the case of ZUWA station in (c), where the red ellipses represent the error estimate for the whole set of individual RF, green ellipses error estimate for the receiver functions with backazimuth > 140^0 (ZUWA S-W) and blue ellipses for the receiver functions with backazimuth < 106^0 (ZUWA N-E).

References

Al-Damegh, K., Sandoval, E. & Brazangi, M., 2005. Crustal structure of the Arabian plate: new constraints from the analysis of teleseismic receiver functions. Earth Planet. Sci. Lett., 231, 177–196.

Ammon, C. J., 1991. The isolation of receiver effects from teleseismic P waveforms, Bull. Seism. Soc. Am., 81, 2504-2510.

Efron, B. & Tibshirani, R., 1986. The Bootstrap Method for standard errors, confidence intervals, and other measures of statistical accuracy. Statistical Sci., 1, No. 1, 1-35.

Egloff, F., Rihm, R., Makris, J., Izzeldin, Y.A., Bobsien, M., Meier, K., Junge, I., Noman, T. & Warsi, W., 1991. Contrasting structural styles of the eastern and westernmargins of the southern Red Sea: the 1988 SONNE experiment. In: J. Makris, P. Mohr and R. Rihm (Editors), Red Sea: Birth and Early History of a New Oceanic Basin. Tectonophysics, 198, 329-353.

Hammond, J. O. S., Kendall, J.M., Stuart, G. W., Keir, D., Ebinger, C. J., Ayele, A. & Belachew, M., 2011. The nature of the crust beneath the Afar triple junction: Evidence from receiver functions. Geochem. Geophys. Geosyst., 12, doi:10.1029/2011GC003738.

Sambridge, M,. 1999a. Geophysical inversion with a neighbourhood algorithm-I. Searching a parameter space. Geophys. J. Int., 138, 479–94.

Sambridge, M., 1999b. Geophysical inversion with a neighbourhood algorithm-II. Appraising the ensemble. Geophys. J. Int., 138, 727–46.

Shibutani, T., Sambridge, M. & Kennett, B., 1996. Genetic algorithm inversion for receiver functions with application to crust and uppermost mantle structure beneath Eastern Australia. Geophys. Res. Lett. 23(14): doi: 10.1029/96GL01671. issn: 0094-8276.

Tiberi, C., Leroy, S., d'Acremont, E., Bellahsen, N., Ebinger, C., Al-Lazki, A. & Pointu, A., 2007. Crustal geometry of the northeastern Gulf of Aden passive margin: localization of the deformation inferred from receiver function analysis. Geophys. J. Int., 168(doi:10.1111/j.1365-246X.2006.03294.x): 1247-1260.

Zhu, L. & Kanamori, H., 2000. Moho Depth Variation in Southern California from Teleseimic Receiver Function. J.Geophys. Res., 105, 2969-2980.

Shibutani, T., Sambridge, M. & Kennett, B., 1996. Genetic algorithm inversion for receiver functions with application to crust and uppermost mantle structure beneath Eastern Australia. Geophys. Res. Lett. 23(14): doi: 10.1029/96GL01671. issn: 0094-8276.

Fig. (S1)

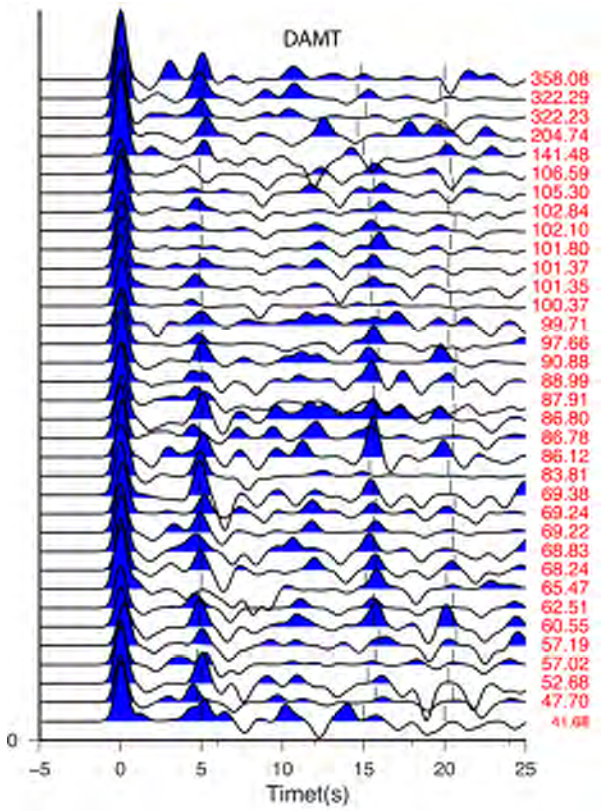
DAMT
358.08
322.29
322.23
204.74
141.48
106.59
105.30
102.84
102.10
101.80
101.37
101.35
100.37
99.71
97.66
90.88
88.99
87.91
86.80
86.78
86.12
83.81
69.38
69.24
69.22
68.83
68.24
65.47
62.51
60.55
57.19
57.02
52.68
47.70
0
−5
0
5
10
15
20
25
Timet(s)

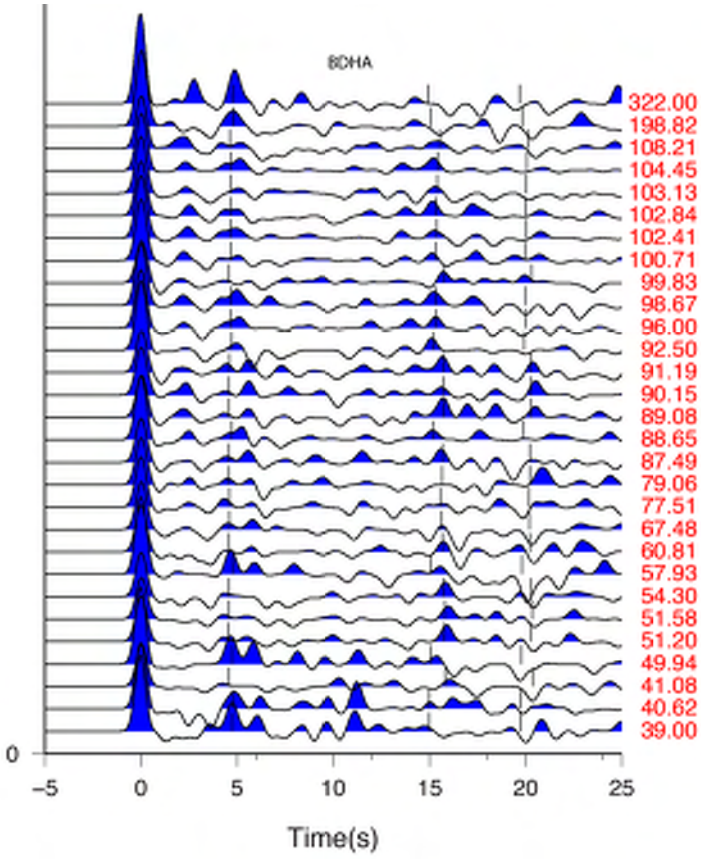
BDHA
322.00
198.82
108.21
104.45
103.13
102.84
102.41
100.71
99.83
98.67
96.00
92.50
91.19
90.15
89.08
88.65
87.49
79.06
77.51
67.48
60.81
57.93
54.30
51.58
51.20
49.94
41.08
40.62
39.00
0
−5
0
5
10
15
20
25
Time(s)

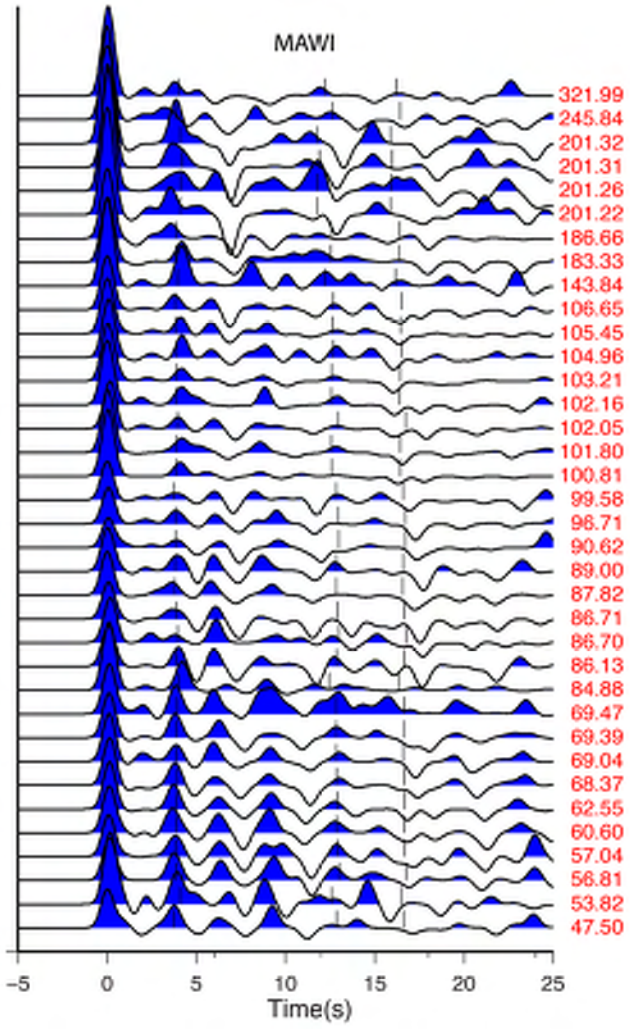
MAWI
321.99
245.84
201.32
201.31
201.26
201.22
186.66
183.33
143.84
106.65
105.45
104.96
103.21
102.16
102.05
101.80
100.81
99.58
96.71
90.62
89.00
87.82
86.71
86.70
86.13
84.88
69.47
69.39
69.04
68.37
62.55
60.60
57.04
56.81
53.82
47.50
−5
0
5
10
15
20
25
Time(s)

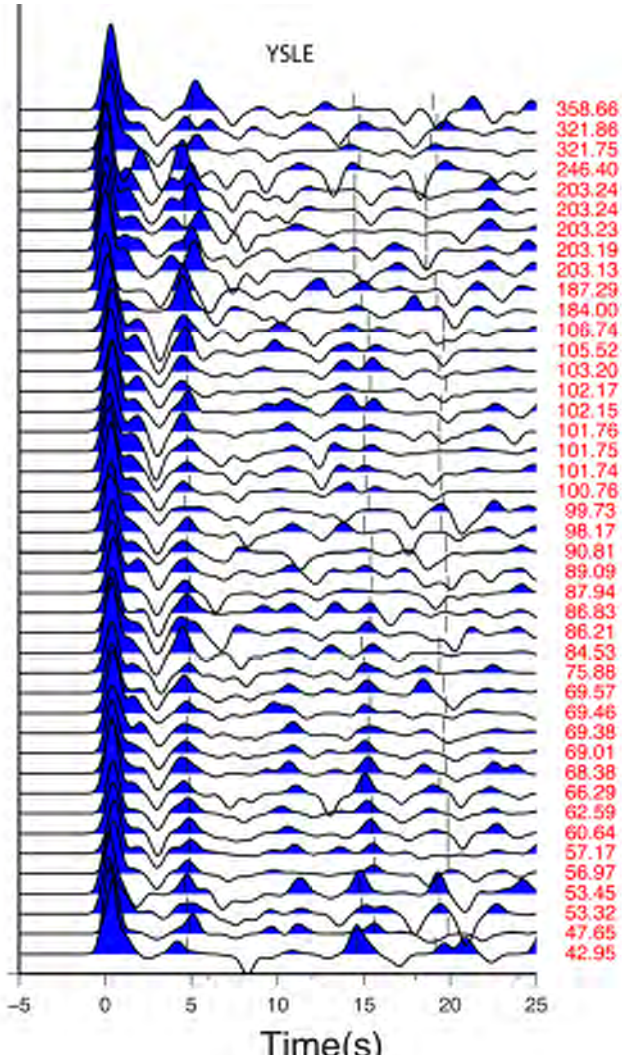
YSLE
358.66
321.86
321.75
246.40
203.24
203.24
203.23
203.19
203.13
187.29
184.00
106.74
105.52
103.20
102.17
102.15
101.76
101.75
101.74
100.76
99.73
98.17
90.81
89.09
87.94
86.83
86.21
84.53
75.88
69.57
69.46
69.38
69.01
68.38
66.29
62.59
60.64
57.17
56.97
53.45
53.32
47.65
42.95
−5
0
5
10
15
20
25
Time(s)

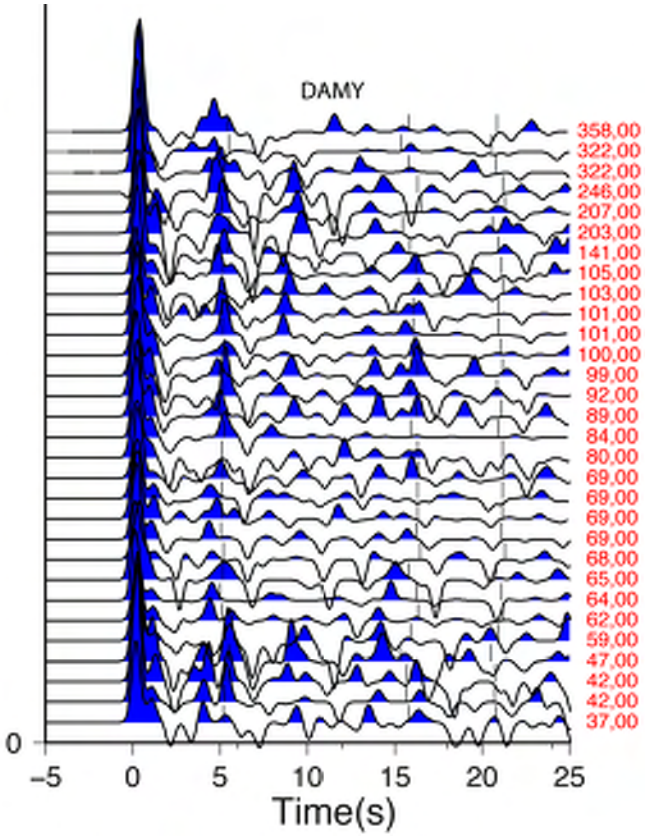
DAMY
358,00
322,00
322,00
246,00
207,00
203,00
141,00
105,00
103,00
101,00
101,00
100,00
99,00
92,00
89,00
84,00
80,00
69,00
69,00
69,00
69,00
68,00
65,00
64,00
62,00
59,00
47,00
42,00
42,00
37,00
0
−5
0
5
10
15
20
25
Time(s)

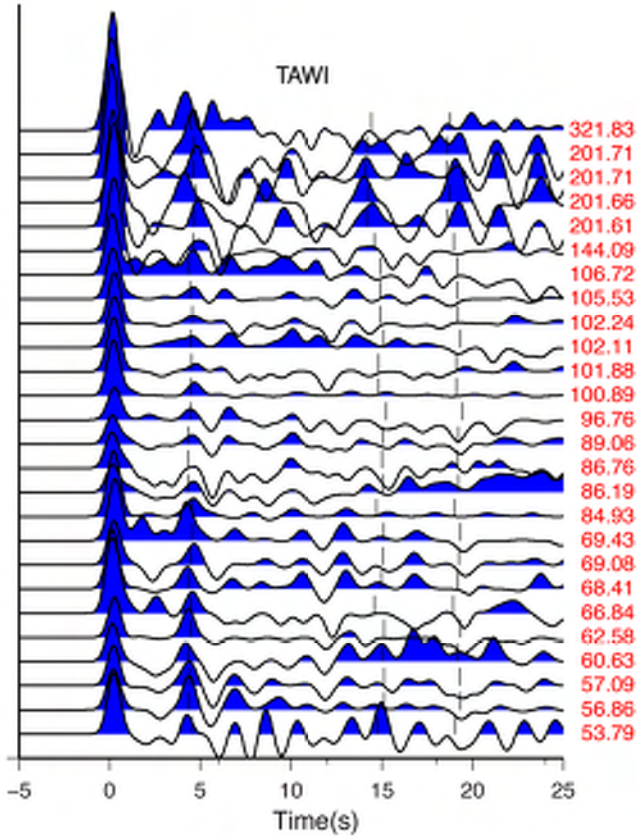
TAWI
321.83
201.71
201.71
201.66
201.61
144.09
106.72
105.53
102.24
102.11
101.88
100.89
96.76
89.06
86.76
86.19
84.93
69.43
69.08
68.41
66.84
62.58
60.63
57.09
56.86
53.79
−5
0
5
10
15
20
25
Time(s)

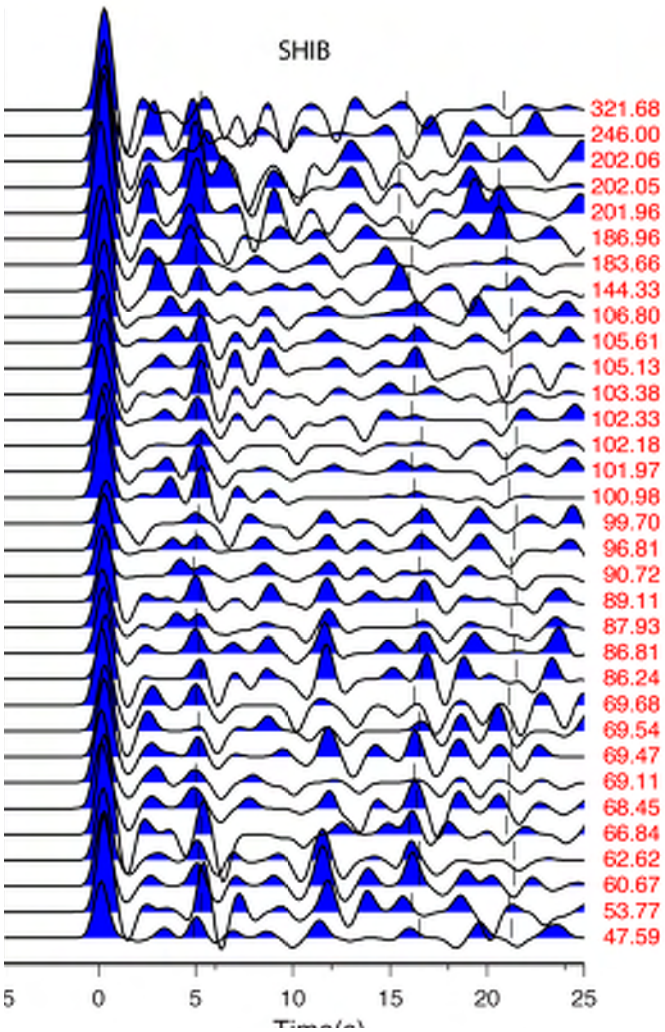
SHIB
321.68
246.00
202.06
202.05
201.96
186.96
183.66
144.33
106.80
105.61
105.13
103.38
102.33
102.18
101.97
100.98
99.70
96.81
90.72
89.11
87.93
86.81
86.24
69.68
69.54
69.47
69.11
68.45
66.84
62.62
60.67
53.77
47.59
5
0
5
10
15
20
25

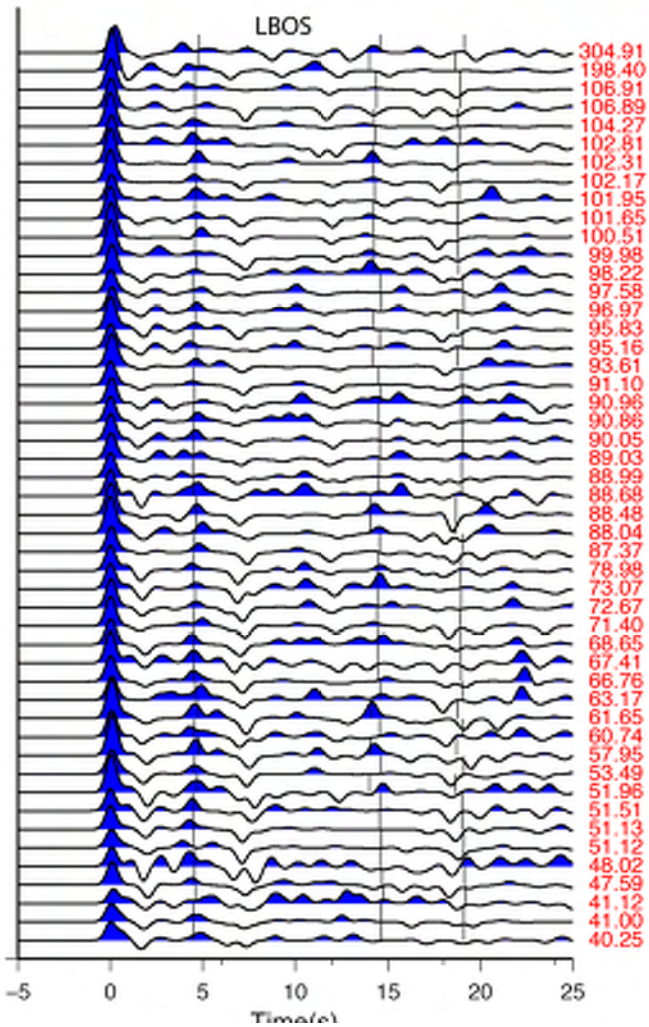
LBOS
304.91
198.40
106.91
106.89
104.27
102.81
102.31
102.17
101.95
101.65
100.51
99.98
98.22
97.58
96.97
95.83
95.16
93.61
91.10
90.96
90.86
90.05
89.03
88.99
88.69
88.48
88.04
87.37
78.98
73.07
72.67
71.40
68.65
67.41
66.76
63.17
61.65
60.74
57.95
53.49
51.96
51.51
51.13
51.12
48.02
47.59
41.12
41.00
40.25
−5
0
5
10
15
20
25

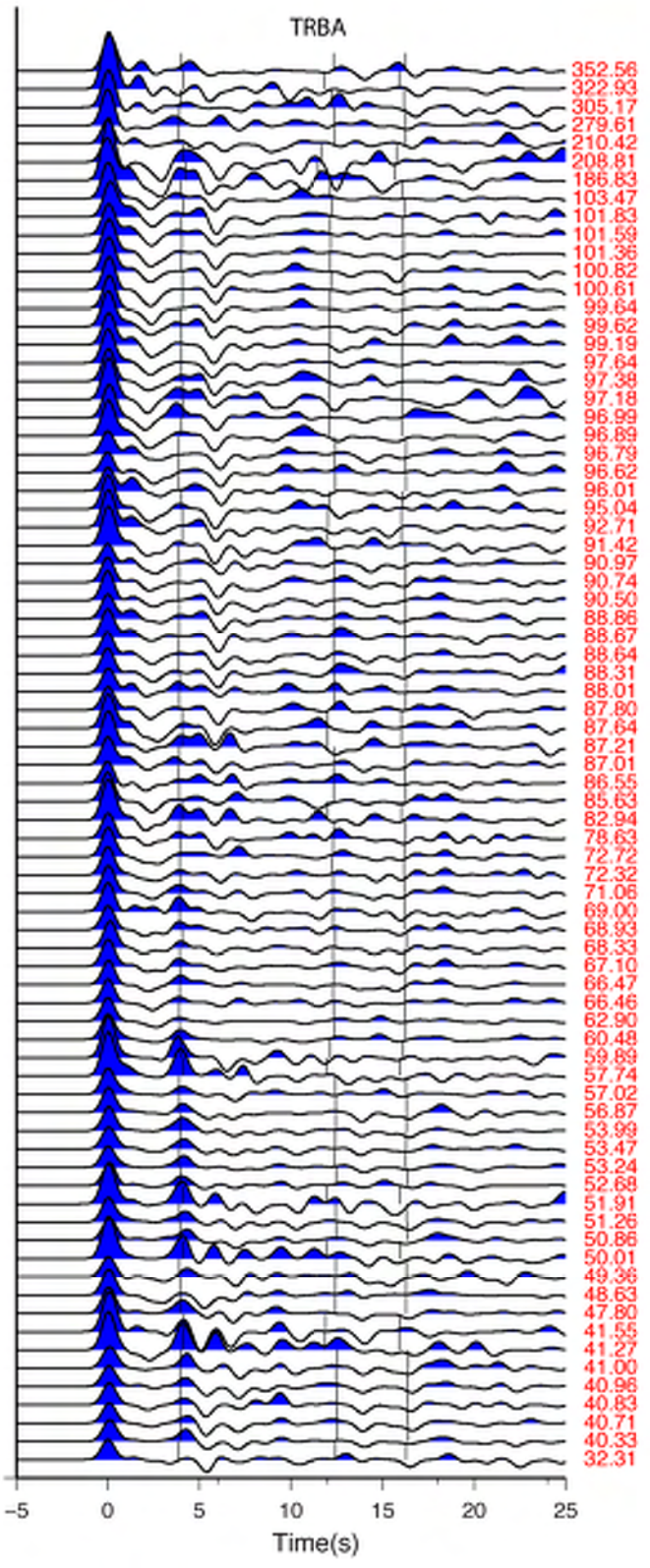
TRBA
352.56
322.93
305.17
279.61
210.42
208.81
186.83
103.47
101.83
101.59
101.36
100.82
100.61
99.64
99.62
99.19
97.64
97.38
97.18
96.99
96.89
96.79
96.62
96.01
95.04
92.71
91.42
90.97
90.74
90.50
88.86
88.67
88.64
88.31
88.01
87.80
87.64
87.21
87.01
86.55
85.63
82.94
78.63
72.72
72.32
71.06
69.00
68.93
68.33
67.10
66.47
66.46
62.90
60.48
59.89
57.74
57.02
56.87
53.99
53.47
53.24
52.68
51.91
51.26
50.86
50.01
49.36
48.63
47.80
41.55
41.27
41.00
40.96
40.83
40.71
40.33
32.31
−5
0
5
10
15
20
25
Time(s)

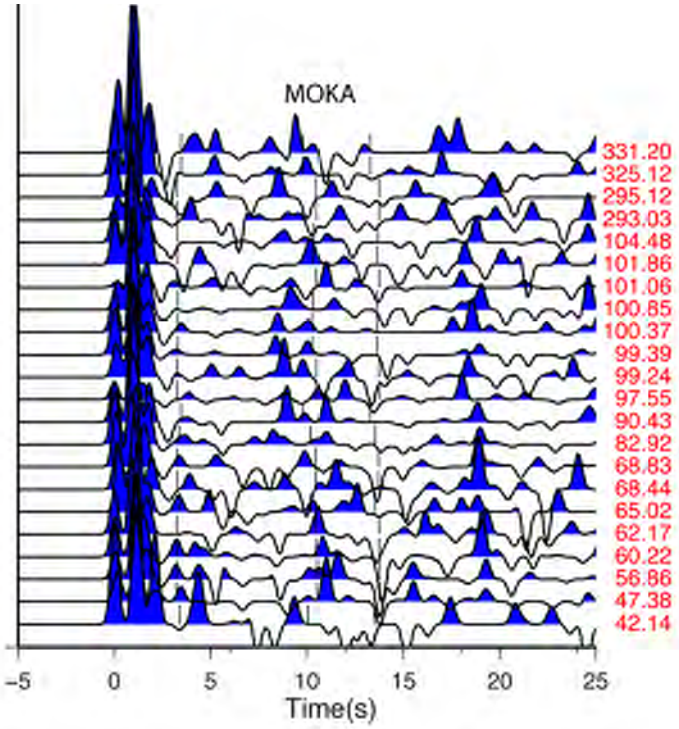
MOKA
331.20
325.12
295.12
293.03
104.48
101.86
101.06
100.85
100.37
99.39
99.24
97.55
90.43
82.92
68.83
68.44
65.02
62.17
60.22
56.86
47.38
42.14
−5
0
5
10
15
20
25
Time(s)

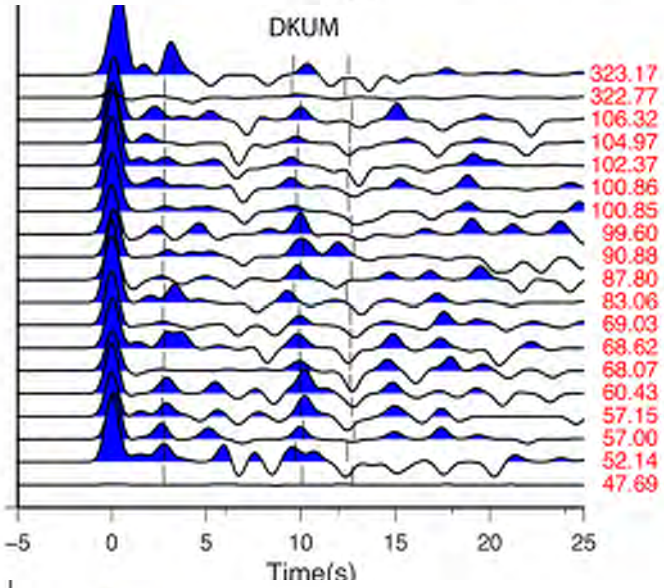
DKUM
323.17
322.77
106.32
104.97
102.37
100.86
100.85
99.60
90.88
87.80
83.06
69.03
68.62
68.07
60.43
57.15
57.00
52.14
47.69
−5
0
5
10
15
20
25
Time(s)

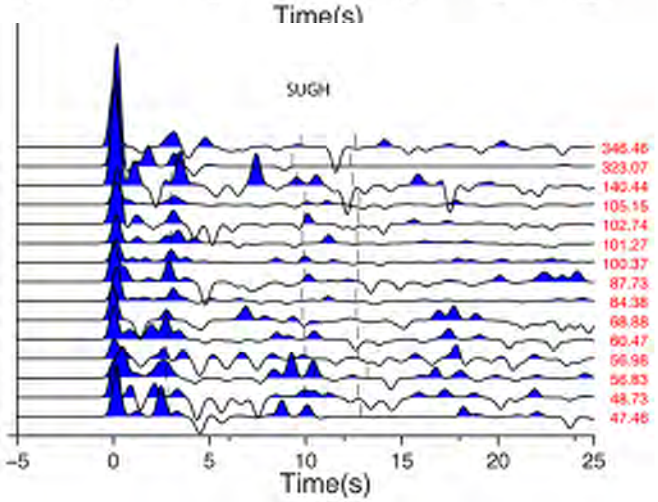
SUGH
346.46
323.07
140.44
105.15
102.74
101.27
100.37
87.73
84.38
68.88
60.47
56.98
56.83
48.73
47.46
−5
0
5
10
15
20
25
Time(s)

Fig. (S2)

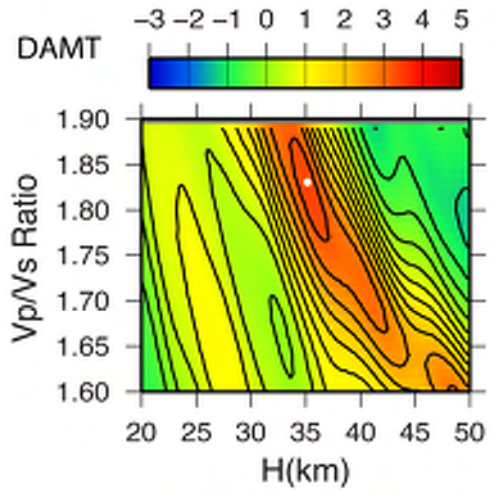
DAMT
−3 −2 −1 0 1 2 3 4 5
Vp/Vs Ratio
1.90 1.85 1.80 1.75 1.70 1.65 1.60
20 25 30 35 40 45 50
H(km)

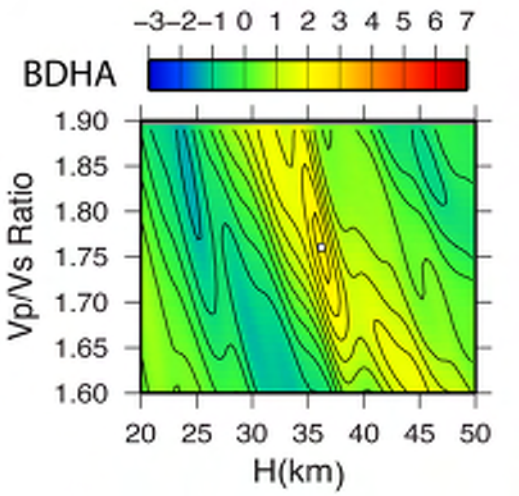
BDHA
−3 −2 −1 0 1 2 3 4 5 6 7
Vp/Vs Ratio
1.90 1.85 1.80 1.75 1.70 1.65 1.60
20 25 30 35 40 45 50
H(km)

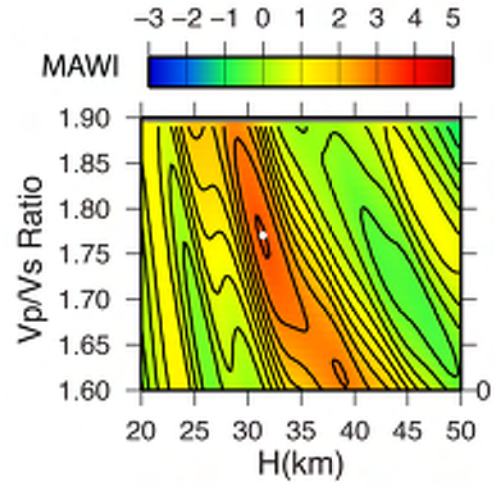
MAWI
−3 −2 −1 0 1 2 3 4 5
Vp/Vs Ratio
1.90 1.85 1.80 1.75 1.70 1.65 1.60
20 25 30 35 40 45 50
H(km)

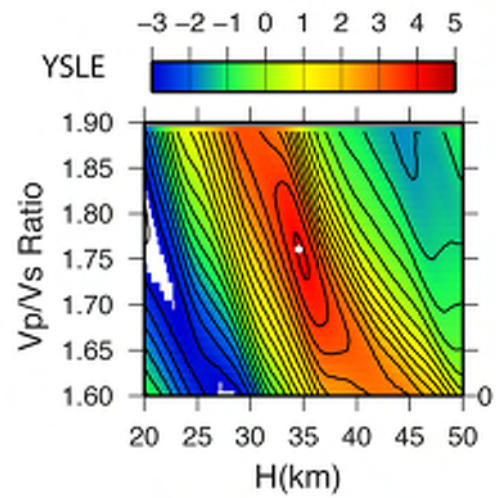
YSLE
−3 −2 −1 0 1 2 3 4 5
Vp/Vs Ratio
1.90 1.85 1.80 1.75 1.70 1.65 1.60
20 25 30 35 40 45 50
H(km)

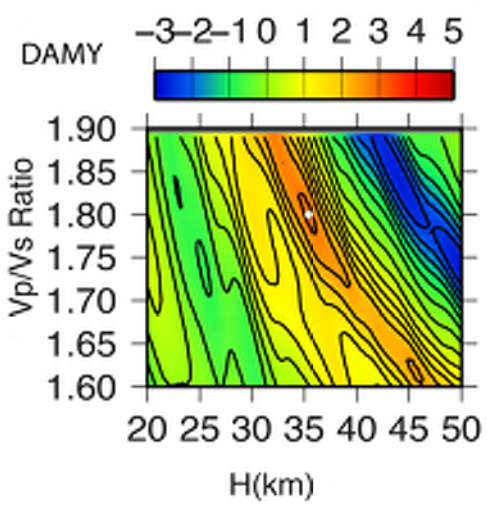
DAMY
−3 −2 −1 0 1 2 3 4 5
Vp/Vs Ratio
1.90 1.85 1.80 1.75 1.70 1.65 1.60
20 25 30 35 40 45 50
H(km)

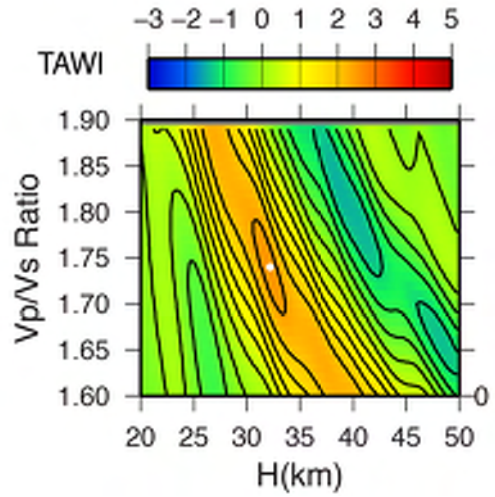
TAWI
−3 −2 −1 0 1 2 3 4 5
Vp/Vs Ratio
1.90 1.85 1.80 1.75 1.70 1.65 1.60
20 25 30 35 40 45 50
H(km)

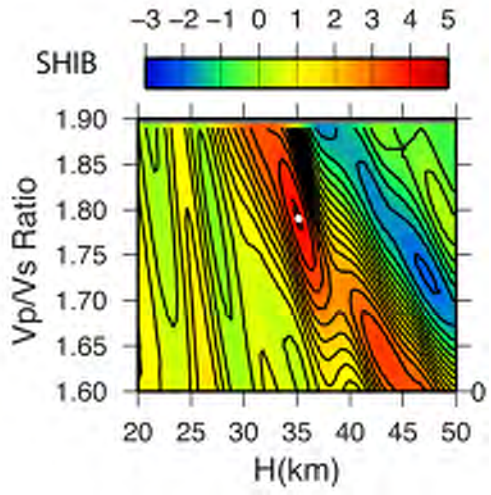
SHIB
−3 −2 −1 0 1 2 3 4 5
Vp/Vs Ratio
1.90
1.85
1.80
1.75
1.70
1.65
1.60
20 25 30 35 40 45 50
H(km)
0

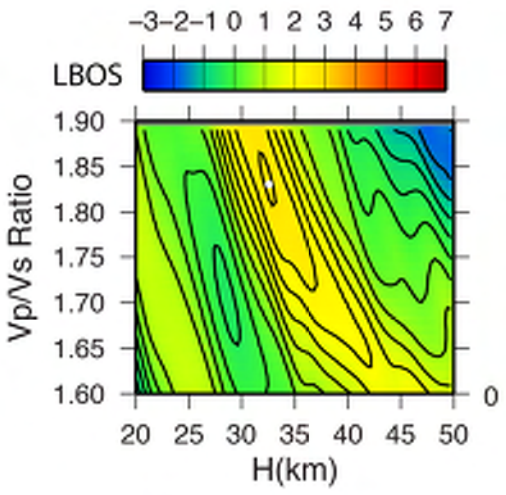
LBOS
−3 −2 −1 0 1 2 3 4 5 6 7
Vp/Vs Ratio
1.90
1.85
1.80
1.75
1.70
1.65
1.60
20 25 30 35 40 45 50
H(km)
0

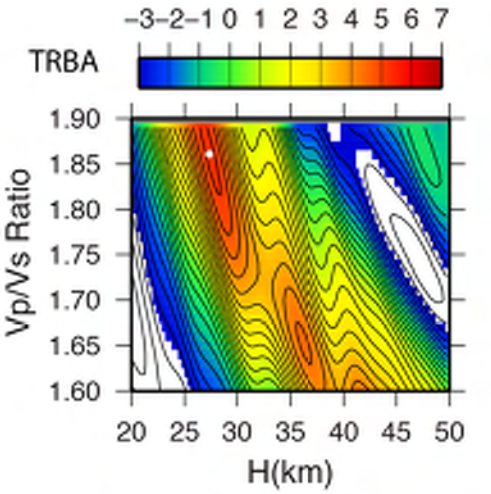
TRBA
−3 −2 −1 0 1 2 3 4 5 6 7
Vp/Vs Ratio
1.90
1.85
1.80
1.75
1.70
1.65
1.60
20 25 30 35 40 45 50
H(km)

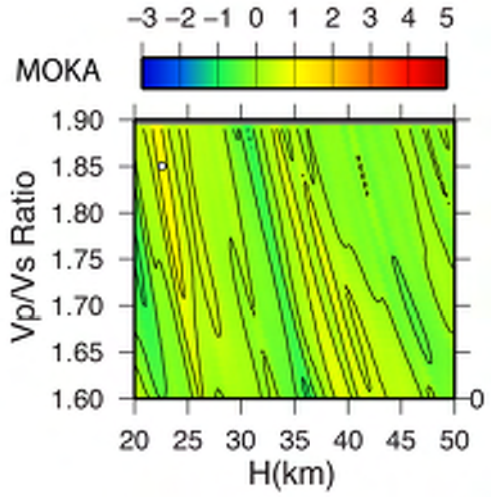
MOKA
−3 −2 −1 0 1 2 3 4 5
Vp/Vs Ratio
1.90
1.85
1.80
1.75
1.70
1.65
1.60
20 25 30 35 40 45 50
H(km)
0

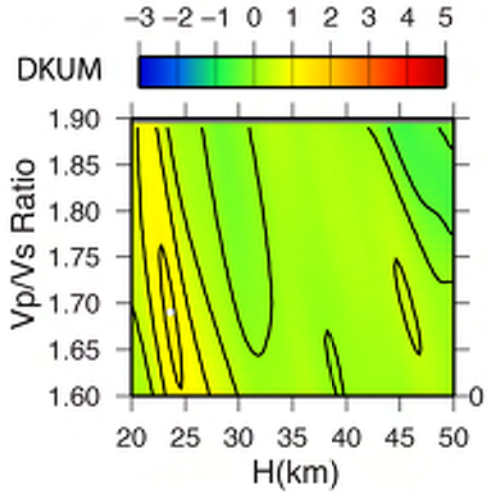
DKUM
−3 −2 −1 0 1 2 3 4 5
Vp/Vs Ratio
1.90
1.85
1.80
1.75
1.70
1.65
1.60
20 25 30 35 40 45 50
H(km)
0

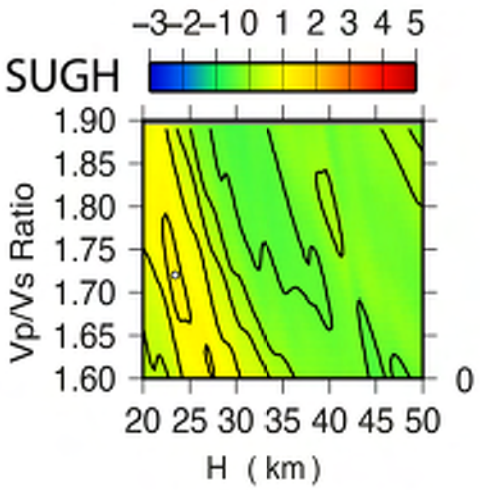
SUGH
−3 −2 −1 0 1 2 3 4 5
Vp/Vs Ratio
1.90
1.85
1.80
1.75
1.70
1.65
1.60
20 25 30 35 40 45 50
H (km)
0

Fig.(S3)

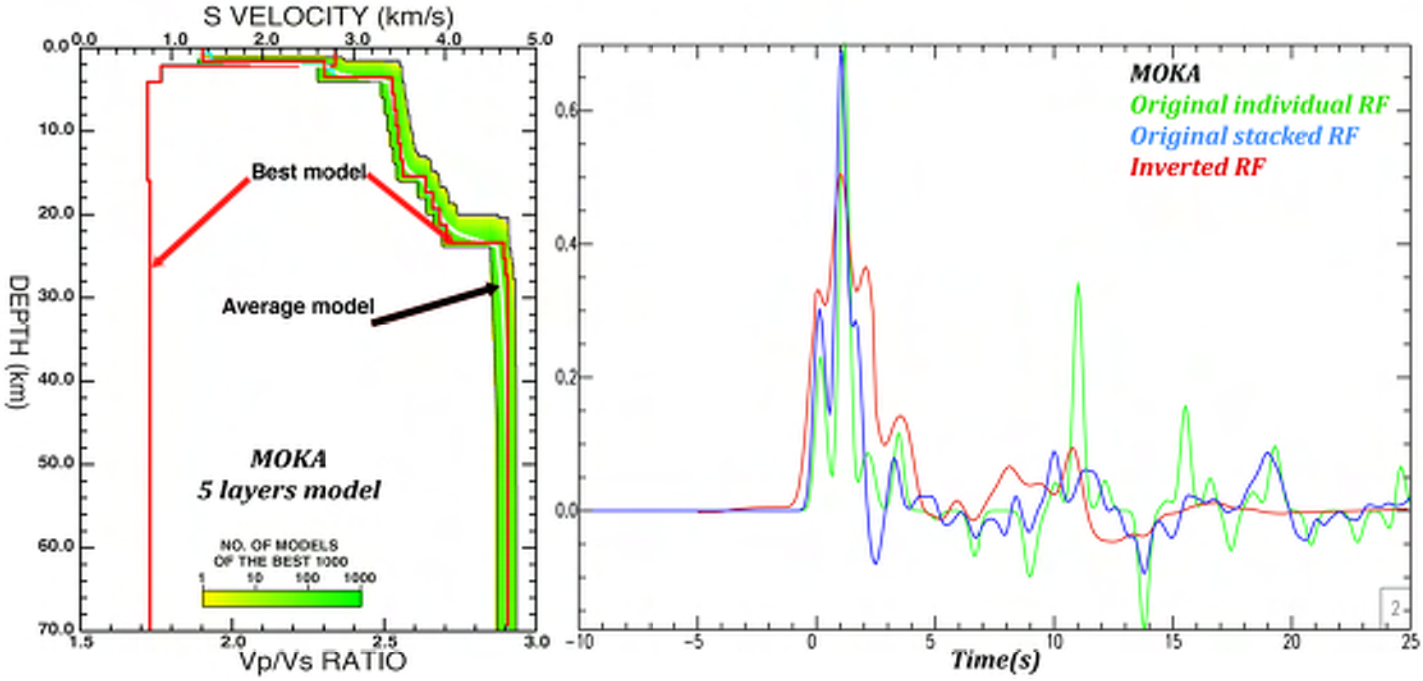

Fig.(S4)

a)

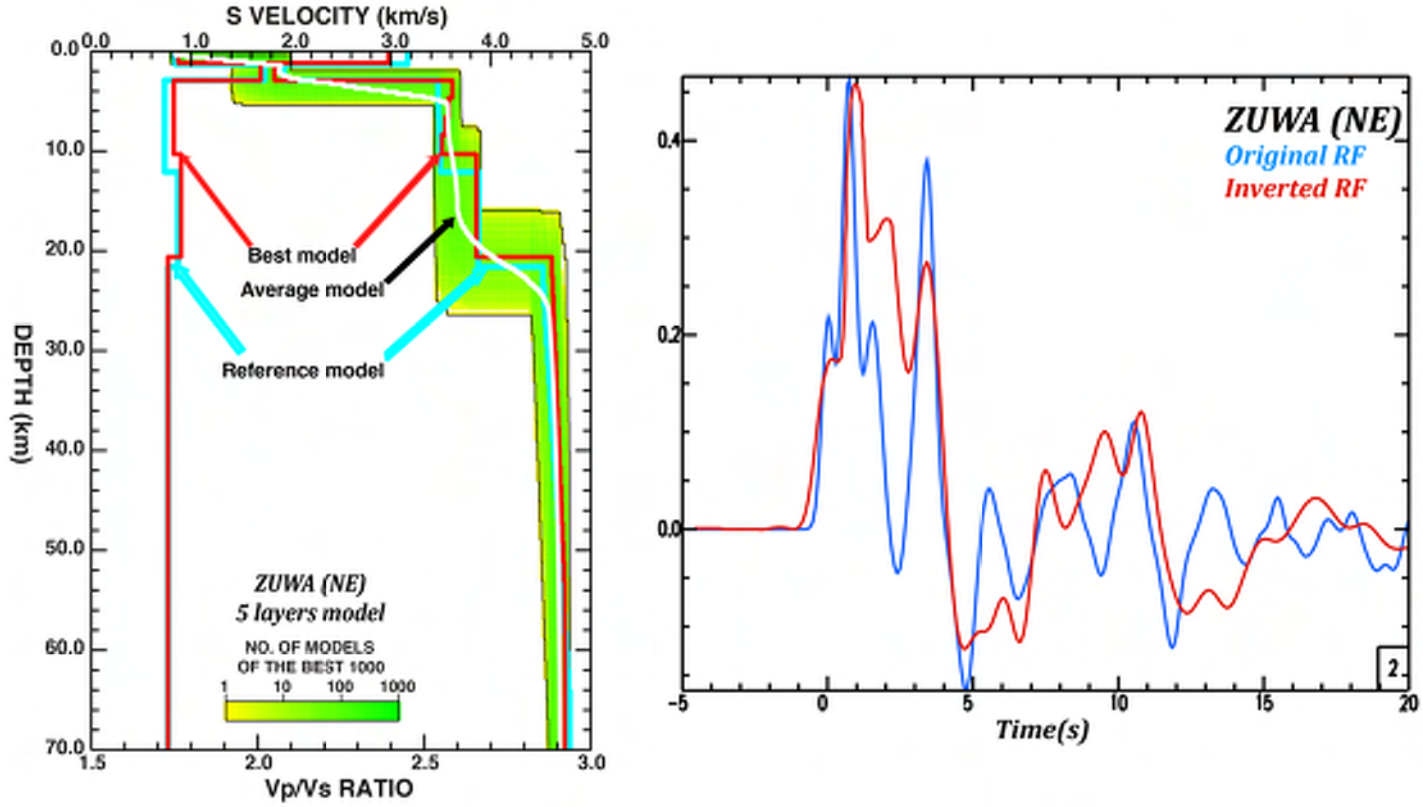

b)

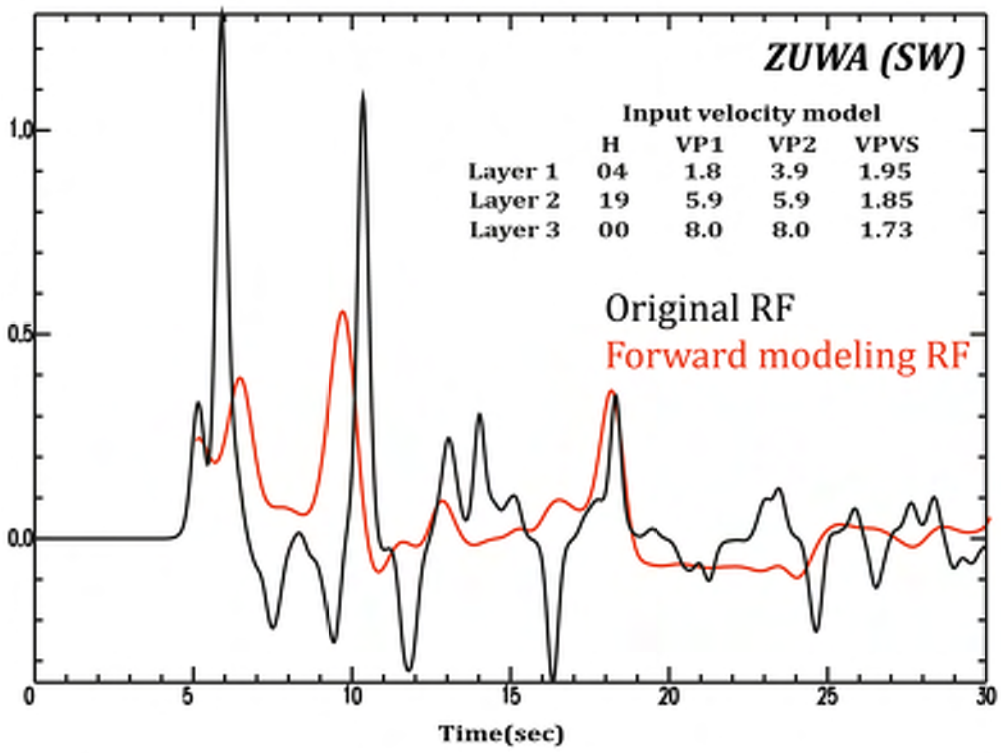
ZUWA (SW)
Input velocity model
H VP1 VP2 VPVS
Layer 1 04 1.8 3.9 1.95
Layer 2 19 5.9 5.9 1.85
Layer 3 00 8.0 8.0 1.73
Original RF
Forward modeling RF
Time(sec)

a) **Fig.(S5)**

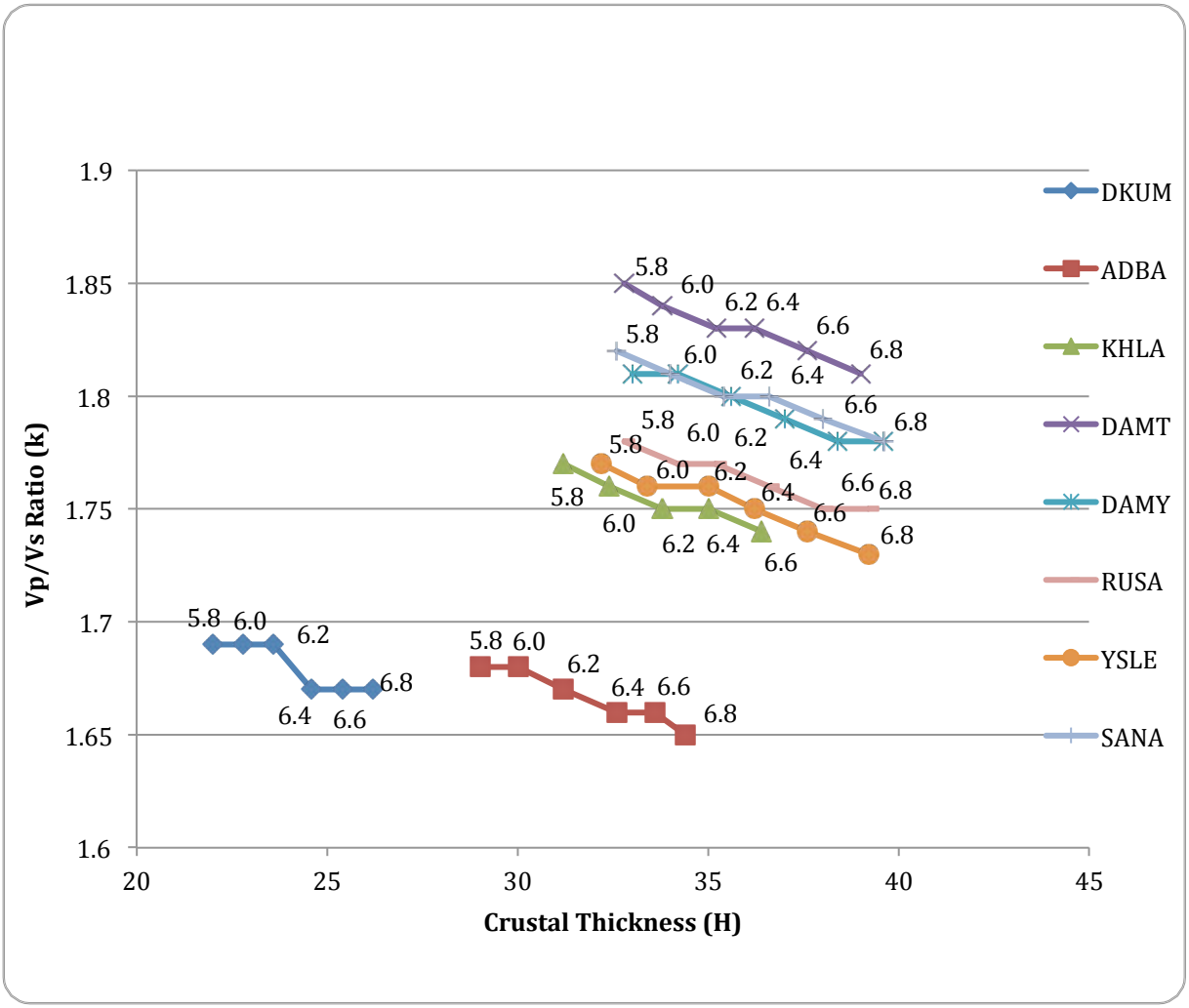
Vp/Vs Ratio (k)
Crustal Thickness (H)
DKUM
ADBA
KHLA
DAMT
DAMY
RUSA
YSLE
SANA

b)

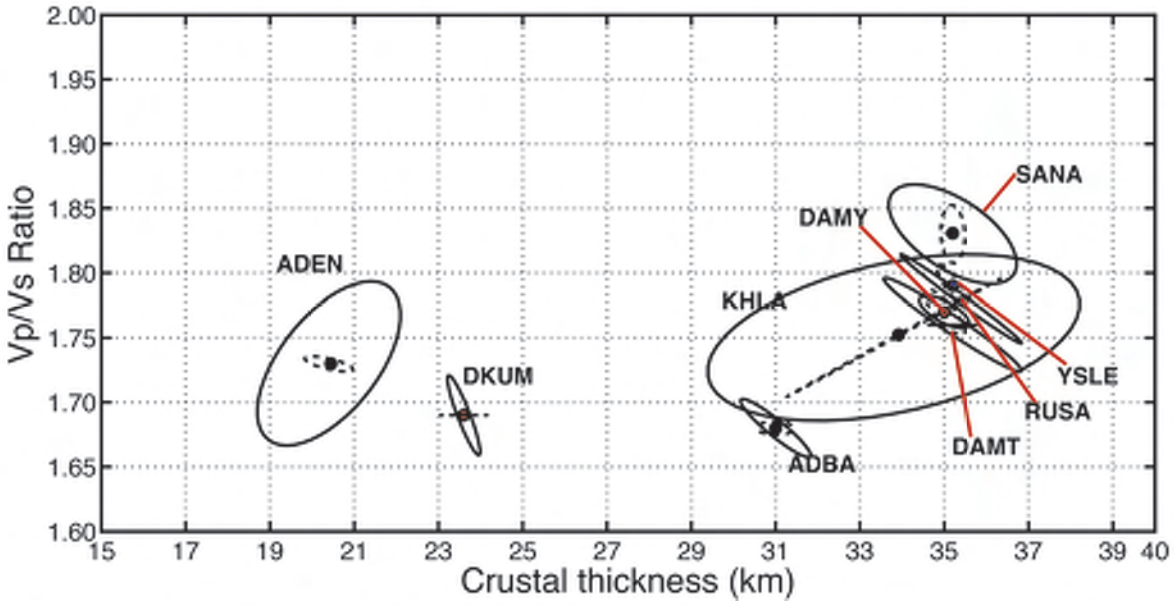
Vp/Vs Ratio
Crustal thickness (km)
ADEN
DKUM
KHLA
DAMY
SANA
YSLE
RUSA
DAMT
ADBA

c)

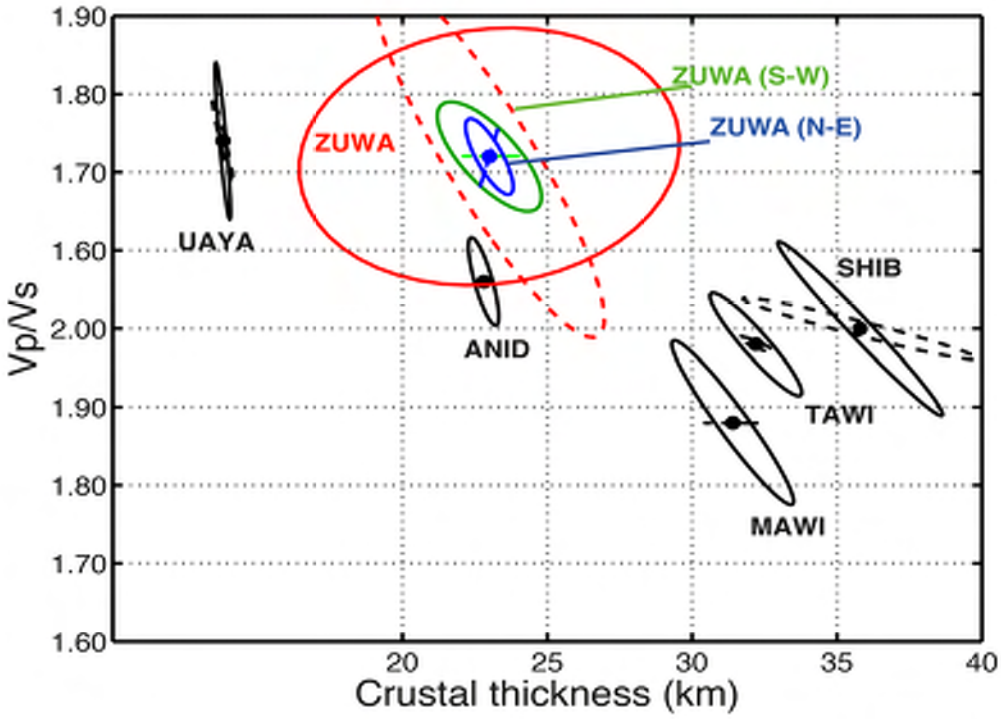
Vp/Vs
Crustal thickness (km)
ZUWA (S-W)
ZUWA (N-E)
ZUWA
UAYA
ANID
SHIB
TAWI
MAWI

d)

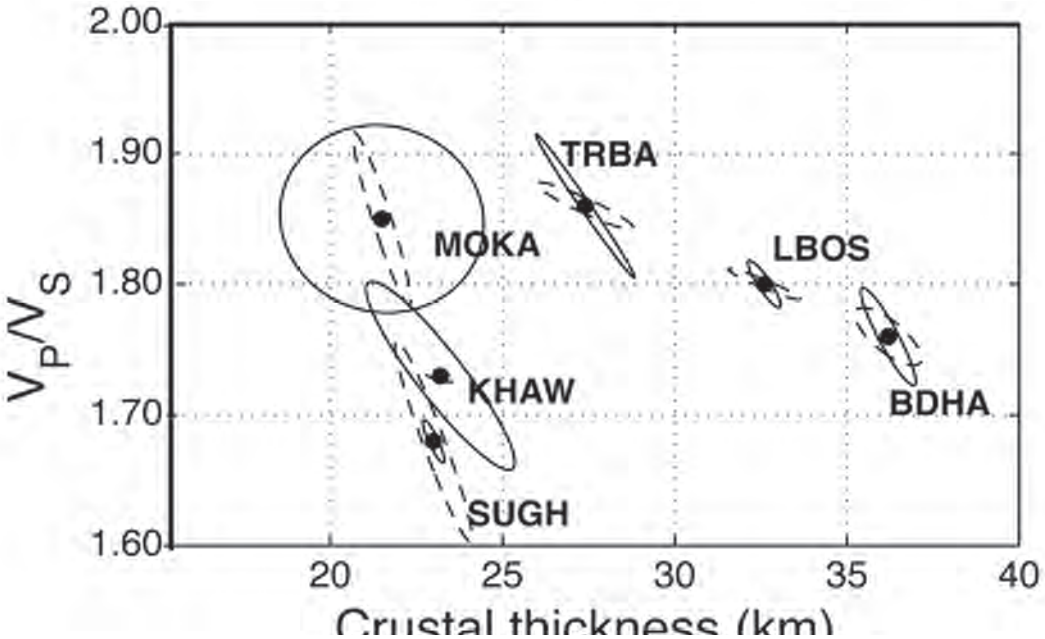
V_P/V_S
Crustal thickness (km)
TRBA
MOKA
LBOS
KHAW
BDHA
SUGH